Large-scale flow of Indian Ocean asthenosphere driven by Réunion plume

G. Barruol*[1,2], K. Sigloch[3], J.-R. Scholz[1,2], A. Mazzullo[1], E. Stutzmann[1], J.-P. Montagner[1], S. Kiselev[4], F. R. Fontaine[1,2], L. Michon[1,2], C. Deplus[1], J. Dyment[1]

1. Université de Paris, Institut de physique du globe de Paris, CNRS, UMR 7154, F-75005 Paris, France

2. Université de La Réunion, Laboratoire GéoSciences Réunion, F-97744 Saint Denis, France

3. University of Oxford, Earth Sciences Department, South Parks Road, Oxford OX1 3AN, UK.

4. Institute of Physics of the Earth, Moscow, Russia

Guilhem Barruol	https://orcid.org/0000-0002-4049-2375
Karin Sigloch	https://orcid.org/0000-0002-9876-4628
John-Robert Scholz	https://orcid.org/0000-0003-1404-2335
Alessandro Mazzullo	https://orcid.org/0000-0003-3844-4312
Jean-Paul Montagner	https://orcid.org/0000-0001-9958-3012
Eléonore Stutzmann	https://orcid.org/0000-0002-4348-7475
Laurent Michon	https://orcid.org/0000-0002-4486-5378
Sergey Kiselev	http://orcid.org/0000-0003-2285-5862
Fabrice R. Fontaine	https://orcid.org/0000-0003-2015-0770
Jérôme Dyment	https://orcid.org/0000-0002-7677-0541

Volcanic hotspot islands are thought to be surface manifestations of mantle plumes rising from the core-mantle boundary. When mantle plumes approach the surface, their mostly vertical rise must be deflected into near-horizontal flow beneath tectonic plates. This creates an opportunity to constrain their dynamics and their interactions with lithospheric plates and mid-ocean ridges. Seafloor observations have been used to propose that focused flow in the asthenosphere transports plume heat to the nearest mid-ocean ridge, where it efficiently dissipates through formation of lithosphere. Here, we present imaging results from a seismological survey of a proposed plume-to-ridge flow channel between the Réunion hotspot and the Central Indian Ridge. Rayleigh-wave tomography and shear-wave splitting confirm the presence of channelized flow of shallow asthenosphere, eastward from hotspot to spreading ridge. At larger scale, a deeper reservoir of hot asthenosphere fills vast tracts of Indian Ocean basin east and north of Réunion Island. Its flows decoupled from overlying lithospheres are also directed toward the Central Indian Ridge but extend well beyond, tapped but not significantly depleted by the spreading ridge. Based on seismic and geochemical observations, we suggest that this hidden heat reservoir is generated and driven by the hotspot, which buffers more heat near the surface than expected.

Since Morgan's (1970) proposal of the deep convection plume hypothesis[1], Réunion has been a prime candidate for expressing such a deeply rooted, “primary" mantle upwelling[1,2]. The island (Fig. 1) is among the most active volcanoes globally, featuring hotspot-type, enriched geochemistry. It is located >1000 km from the closest plate boundary at the young end of a 5500-km long, time-progressive volcanic track that emerged from the Deccan flood basalts of India ~65 millions years ago[1,3,4]. The lowermost mantle under the region is anomalously slow in global tomography models[5-7], consistent with upwelling from the core-mantle boundary, but a surface connection has remained debateable due to insufficient seismic imaging resolution in the mid- and upper mantle, as for other oceanic hotspots. Morgan complemented his deep plume hypothesis by the prediction that upwelling plumes, acting as a heat source near the surface, may establish a vigorous connection to nearby spreading ridges (heat sinks), via pipeline-like flow in the asthenosphere[8]. Citing the Réunion, Galapagos, and Kerguelen systems as examples, he postulated such plume-ridge interaction for all hotspots that had spawned and initially captured a spreading ridge, which subsequently "escaped" to a moderate distance. Réunion's pipeline would have developed when the CIR gradually moved away and east of Réunion after 34 Ma[8,9,10]. Supporting surface evidence of plume-ridge interaction includes:

i) Rodrigues Ridge (Fig. 1a) - an aseismic, east-west striking bathymetric high that projects the connection over time between Réunion’s hotspot track and the CIR – presumably formed through volcanic upward leakage of channel flow, from at least 7-10 My ago[4] to 1.5 My[11];

ii) Hotspot signature in the nearest CIR segment between Marie Celeste and Egeria Fault Zones (~17°-21°S). The segment protrudes westward, is exceptionally long, unusually elevated and asymmetric, with smoother bathymetry on its western ridge flank (Fig. 1a) - all suggesting preferential, hot feeding from Réunion;

iii) Réunion hotspot signature[12-15] in the major- and trace-elements and isotopic compositions of basalts dredged on the CIR between 18°S-21°S, and on easternmost Rodrigues Ridge (Gasitao and Three Magi Ridges);

iv) Slow earthquakes on Marie Celeste transform fault, which could indicate the presence of lubricating, hotspot-generated melts[16].

Seismological imaging of lithosphere and asthenosphere

The RHUM-RUM experiment[17] (Réunion Hotspot and Upper Mantle - Réunions Unterer Mantel, http://www.rhum-rum.net/) instrumented the area of Fig. 1a with 57 broadband ocean-bottom seismometers (OBS) for 13 months, and with 20 island stations for 2-4 years (details in Methods). The largest oceanic plume imaging effort to date in terms of area and instruments deployed simultaneously, RHUM-RUM also represents the first long-term deployment above one of Morgan's hypothesized asthenospheric flow channels[8].

To infer patterns of heat and material flow in the upper 300 km, we combine the complementary methods of anisotropic surface-wave tomography (fundamental-mode Rayleigh waves, 30-300s)[18] and shear-wave splitting measurements[19]. Isotropic shear-velocity anomalies (*dVs/Vs*) are a proxy primarily for mantle temperature, and azimuthal anisotropy of *dVs/Vs* a proxy for current or past mantle flow. Compared to the previously very sparse seismic instrumentation, RHUM-RUM substantially improved seismic resolution across much of the Indian Ocean basin (Supplementary Fig. S1).

Beneath the CIR, tomography[18] shows a band of slower-than-average *dVs/Vs* at 50-90 km depth (red in Fig. 1b-f), as expected from thin or absent lithosphere. Réunion and Mauritius are underlain by faster-than-average shear velocities down to ~60 km depth (dark blue in Fig. 1b/c), consistent with 60-90 million year old lithosphere in the Mascarene Basin[20].

Under the Rodrigues corridor, which stretches ~1000 km from Réunion to the CIR, the asthenosphere reaches closer to the surface than to its north or south. From 50-90 km depth in Fig. 1b-f, this tongue of slow asthenosphere protrudes progressively westward from the anomalous CIR segment, deepening to 80-90 km under Réunion. The tongue's north-south width of ~400 km is resolved (see Methods and Supplementary Fig. S2 and S3), and roughly matches the north-south extent of the anomalous CIR segment (~17°-21°S, Fig. 1a).

On the larger scale of the Indian Ocean basin, Fig. 2 presents the tomography model and Fig. 3a maps lithospheric thickness, or depth of the lithosphere-asthenosphere boundary (LAB), estimated as the 1200°C isotherm derived from isotropic *dVs/Vs*[21] (see Methods and Fig. S6). Lithosphere is observed to thicken perpendicularly away from the CIR, i.e., with seafloor age, as expected for conductive halfspace cooling. The east-west "groove" of thinned Rodrigues corridor lithosphere in Fig. 3a, with its gentler thickening gradient and shallowing asthenosphere (Fig. 2b&c), is unexpected and must reflect additional heat flux.

Apart from Rodrigues corridor, slow *dVs/Vs* anomalies in the upper 100 km in Fig. 2b/c correlate strongly with the Indian Ocean's four spreading ridges (Carlsberg, Central, Southwest and Southeast Indian Ridges). This predictable pattern changes completely below 100 km, where the mid-ocean ridges are not or only slightly slow along much of their length (Fig. 2d, e, f). Instead, slow asthenosphere is abundant beneath the eastern half of the Somali plate, stretching east and northeast of Madagascar and towards the CIR. Below 200 km, this vast slow anomaly is centred beneath the Mascarene Basin, where it bottoms out at or below 350 km, our deepest resolvable depth.

Discernible in some previous tomographies[22,23], this basin-sized body of slow asthenosphere has come in sharp focus through the dense RHUM-RUM data (Supplementary Fig. S1). We term it “Mascarene Basin Asthenospheric

Reservoir" (MBAR) and its connectivity across depths is highlighted by Fig. 3b, a three-dimensional rendering of slow anomalies located deeper than 100 km (which eliminates spreading ridges). The MBAR extends north and east of Réunion, its southern limit coinciding with Rodrigues corridor. At latitudes ~6°-17°S, MBAR spills beneath the CIR and across to the Indo-Australian plate but does not extend to the region's other spreading centres, i.e., the Rodrigues triple junction, Southwest Indian Ridge, East African Rift System (Fig. 2d-f and Fig. 3b).

Asthenospheric flow inferred from seismic anisotropy

Seismic anisotropy is dominantly controlled by the alignment of olivine crystals' fast axis [100] in flow direction[24,25] (details in Methods), thus constituting a proxy for upper-mantle flow.

Beneath seismic stations, azimuthal anisotropy is robustly constrained by 88 SKS splitting measurements[19], which provide high lateral resolution of ~50 km, but little vertical resolution (Fig. 1a). Fast S-velocity directions strike roughly east-west under Rodrigues corridor, consistent across OBS and with earlier measurements on Réunion, Mauritius and Rodrigues island stations[26] (Fig. 1a). Along a central axis connecting Mauritius, Rodrigues, and the CIR, fast directions strike almost exactly east-west. North of this axis, they have a south-pointing component (N100°E), whereas south of it, anisotropy points slightly north (N80°E). West of Réunion, fast directions wrap around the leading edge of the hotspot track. Jointly these splitting observations suggest a latitudinal gathering of eastward flow, from relatively diffuse in the Mascarene Basin into a focused stream towards the spreading ridge, at least as wide as the instrumented area (~400 km latitudinally, Fig. 1a). SKS phases[19] are split by 1-2 s (Fig. 1a), of which 80% probably originates in the asthenosphere (as indicated by forward propagation through the tomography model, see Methods and

155 Supplementary Fig. S7). These substantial splits imply a 100-150 km thick flowing
156 layer, assuming typical intrinsic anisotropy of 3-5% in flowing mantle[25].

157 Rayleigh-wave tomography yields azimuthal anisotropy as a function of
158 depth, extending beyond instrumented areas to the basin scale, but with lower lateral
159 resolution of ~300 km (Supplementary Figs. S2, S3, S5). Tomographically estimated
160 anisotropy is superimposed on depth sections of isotropic *dVs/Vs* in Figs. 1&2, and
161 on a 3-D rendering of the MBAR in Fig. 3b. Within the MBAR (Fig. 2d-f and 3b),
162 anisotropy is strong and aligns E-W to NW-SE, joining up well with SKS splits under
163 northern Rodrigues corridor (Fig. 1a). Anisotropy appears weak and incoherent under
164 the corridor itself (Figs. 2d, 1f), seemingly in contradiction with splitting observations
165 but explained if the (less resolving) surface waves averaged over very different
166 structures within and south of Rodrigues corridor.

167 Stark anisotropy contrasts between MBAR asthenosphere and overlying
168 lithosphere are evident in Figures 2b versus 2d, or 3a versus 3b, but best
169 appreciated in east-west cross-sections (Fig. 4), where bars indicating fast directions
170 are arranged in vertical columns to highlight changes of azimuthal anisotropy with
171 depth. Under the Mascarene Basin and Réunion (red star), lithosphere anisotropy
172 strikes roughly north-south (near-vertical bars), almost perpendicular to
173 asthenospheric anisotropy. The transition in depth is marked by anisotropy minima.
174 Almost everywhere these "zero-crossings" of anisotropy coincide with the
175 isotropically imaged LAB (the sharp vertical transition from blue to red shades), a
176 finding that lends credence to these anisotropy minima as alternative LAB markers.
177 The observed LAB transition spans around 20 km vertically, a sharpness well
178 resolved according to resolution tests (see Methods and Supplementary Fig. S5).

179 Within the isotropically defined asthenosphere (red areas in Fig. 4), fast *Vs*
180 azimuths tend to arrange into spindle-shaped vertical profiles, most clearly expressed
181 in sections 18.5°S and 12.5°S. Anisotropy magnitude peaks in the middle of the

182 slow layer and crosses zero at both its top and bottom. Since the upper minimum
183 marks the LAB, the lower seems to define the elusive asthenosphere-mesosphere
184 boundary, which is poorly defined by isotropic *dVs/Vs*. It is observed between 150-
185 200 km depth across Fig. 4, bounding 100-150 km thick asthenosphere from below.
186 The occurrence of spindle-shaped anisotropy profiles, first reported here to
187 our knowledge, is limited to areas of very slow isotropic *Vs*, i.e., to asthenosphere of
188 the MBAR and the Rodrigues corridor. South of the corridor (21.5°S and 26.5°S),
189 spindles are weakly developed or absent, even though moderately slow *dVs/Vs* still
190 delineates the asthenosphere isotropically.
191 The spindle-shaped anisotropy profiles resemble parabolic velocity profiles of
192 planar, Poiseuille-type flow of fluid between two horizontal confining "plates"
193 (lithosphere and mesosphere). Poiseuille flow is actively driven by a horizontal
194 pressure gradient[27,28], as would be caused by plume upwelling in the west. Assuming
195 anisotropy is caused by strain and hence proportional to the vertical derivative of
196 (horizontal) fluid flow, the parabola-shaped depth profile of Poiseuille flow in
197 isoviscous fluid should generate an anisotropy minimum in the middle of the flow[28,29]
198 (Supplementary Fig. S4), contrary to the actually observed maximum. Real mantle
199 rheologies are, however, nonlinear and temperature-dependent. Hence a viscosity
200 minimum in the middle of the MBAR asthenosphere – compatible with peak isotropic
201 *dVs/Vs* observed there - would concentrate flow and hence anisotropy in the middle
202 of the layer, as observed in Fig. 4 and schematized in Fig. 5 and Supplementary Fig.
203 S4.
204 Alternatively, asthenosphere might be passively dragged by overlying
205 lithosphere, predicting completely different anisotropy profiles (Couette flow,
206 Supplementary Fig. S4). Intuition and geodynamic modelling[30,31] indicate that such
207 asthenospheric flow and anisotropy should be aligned with the (northeastward)
208 motion of the overlying Somali and Indian plates[32,33] (Supplementary Fig. S7), a stark

mismatch to the MBAR's robustly observed, W-E to NW-SE striking anisotropy. Fluid velocities and anisotropy in Couette flow would peak at the LAB and taper downward[27] (Supplementary Fig. S4), as would anisotropy. Our resolution tests (Methods and Supplementary Fig. S5) indicate that such an anisotropy maximum at the LAB can be ruled out and that the observed minimum at the LAB is resolved. Hence our observations robustly support the dominance of actively driven asthenospheric flow, directed (south-)eastward toward the CIR (a sink of asthenosphere) and driven by a westerly source (plume?).

Plume-ridge interaction beneath the Central Indian Ridge

In the lithosphere, fast azimuthal anisotropy is oriented N-S in the Cretaceous-aged Mascarene Basin and NE-SW in seafloor produced by the younger CIR (Fig. 3a), i.e., consistently parallel to (paleo-)spreading directions as expected. Where MBAR asthenosphere spills under the CIR at latitudes ~6°-17°S, a shallow layer of NE-SW anisotropy (parallel to current CIR spreading) is underlain by a layer of NW-SE anisotropy (Fig. 4, clearest at 7.5°S below the green circle, and also at 12.5°S). Unlike everywhere else, this change of anisotropy direction beneath the spreading ridge occurs within the asthenosphere, not at the (isotropic) LAB. Hence the superficial part of the MBAR appears to feed the accreting CIR, re-aligning its flow with the spreading, but the CIR's suction appears too weak to significantly drain or divert the MBAR's deeper, NW-SE directed flow across to the Indo-Australian plate, where additional large areas of slow asthenosphere are imaged (Figs. 2d-f, 3b, 4).

This hypothesis predicts that CIR basalts should sample the hotspot-influenced geochemistries of Rodrigues and MBAR flows. Indeed, basalts dredged in the Rodrigues CIR segment (17°S to 21°S) require mixing between standard MORB and Réunion's ocean island basalt (OIB) signatures[12,13,15,34], and

He^3/He^4 ratios are intermediate between MORB and Réunion OIB[14]. Between 8°S and 12°S, where MBAR passes beneath the CIR, basalts are also enriched but geochemically distinct from Rodrigues corridor samples[34]. Originally interpreted as a mantle upwelling other than Réunion, but also located ~1000 km west of the CIR[34], our observations clarify that this second enriched reservoir is the MBAR.

Under the Rodrigues corridor, all subsurface observations support Morgan's hypothesis of hotspot-ridge interaction[8], as summarized by Fig. 5. The Réunion hotspot supplies hot asthenosphere, which generates a horizontal pressure gradient and Poiseuille-type flow towards the asthenosphere-consuming CIR. This flow is focused by an east-west striking groove of thinned lithosphere, which facilitates leakage of lavas to the surface, explaining the presence of Rodrigues Ridge's thickened crust and geochemical OIB signature. Groove-like thinning is implicit in Morgan's hypothesis, who reconstructed Rodrigues corridor as the persistent line of flow from hotspot to eastward-drifting CIR over time, an evolution that exposed (only) this corridor of lithosphere to prolonged excess heat. Approaching the CIR, the flow channel's hot contents account for the anomalously swelled CIR segment[8,10,35] and its hotspot-influenced geochemistry.

Other examples of "Morgan-type"[8] hotspot-ridge interaction have been investigated from surface evidence, e.g., for Galapagos/Darwin[8,36,37], Kerguelen/Amsterdam[8,16,38], but our results are the first to resolve this relatively small-scale (<1000 km) flow phenomenon in the oceanic subsurface.

Much larger, hidden flow of asthenosphere

Surprisingly, our MBAR observations suggest yet another flow type towards the mid-ocean ridge, which is deeper and much broader than Rodrigues channel flow. Rodrigues corridor marks the MBAR's southern limit (Fig. 3b), and asthenosphere in both is expressed similarly in isotropic and anisotropic S-

velocities, but the lithospheric lid is thicker above the MBAR (Fig. 3 and 4). This may explain the MBAR's limited surface expressions, consisting of an enriched CIR MORB signature[34] and the Mascarene Basin's unexpectedly shallow bathymetry (~500 m residual)[39]. East of the CIR, MBAR flow may also be expressed in plate motion changes of the Capricorn plate[39].

The combination of very slow S-velocities, Poiseuille-type anisotropy profiles unaligned with current plate motion (Supplementary Fig. S7) or CIR spreading, and of enriched CIR basalts strongly suggest that MBAR asthenosphere is fed from some kind of deep upwelling. This could be Réunion's remnant plume head and/or younger plume tail[40]. This origin would have required effective NE-ward dragging of plume asthenosphere by the formerly fast-moving Indian plate (Couette-like flow), unlike the plate-asthenosphere decoupling implied by present-day Poiseuille flow (Methods and SI). Today's fast-moving Pacific plate is indeed known to have motion-parallel, basin-scale fast anisotropy directions[41] and a clear Couette flow component[27,28].

A more intuitive source for the MBAR would be a separate plume rising beneath the Mascarene Basin. This would explain south-eastward anisotropy towards the CIR and enriched MORB compositions at 8°S-12°S that are distinct from Réunion/Rodrigues[34]. However, our ongoing body-wave tomography work[42] indicates no deep upwelling north of Réunion, leaving the possibility of a separate paleo-upwelling under the Mascarene Basin that has since lost its connection to the deep mantle[40].

Below 100 km depth, the vast MBAR connects seamlessly to equally vast areas of slow *dVs/Vs* and pronounced east-west anisotropy under the Indo-Australian plate (Fig. 3b), resembling to asthenospheric fingering[43], imaged by surface-wave tomography beneath the Pacific[44,45] and South Atlantic[46] oceans, other hotspot-rich regions. If all this asthenosphere is indeed sourced from deep mantle

upwelling, the observed continuity of strong anisotropy (i.e., flow) across large tracts of Indian Ocean points in the direction of a plume-fed asthenosphere[47,48]. It implies that the heat brought toward the surface by mantle plumes may remain largely trapped and overlooked beneath the oceans, with little or unexpected surface manifestations[39]. Due to its vast spatial spread, MBAR-like asthenosphere would tend to be perceived as the default state of seismically defined low-velocity asthenosphere in a sparsely instrumented ocean, rather than recognized as a large heat buffer fed by a localized, deep mantle source. Much of this heat would be lost slowly and imperceptibly through conductive half-space cooling of lithosphere overhead, rather than through hotspot volcanism or MOR accretion. Hence the recognition of deep Mascarene Basin asthenosphere as plume-sourced, as argued here from high-resolution seismological observations on the seafloor, calls for an upward revision of the plumes' relative contribution to the earth's heat budget.

References

1. Courtillot V., Davaille A., Besse J. & Stock J. Three distinct types of hotspots in the Earth's mantle. *Earth Planet. Sci. Lett.*, **205**, 295-308 (2003).
2. Morgan W.J. Convection plumes in the lower mantle. *Nature*, **230**, 42-43 (1971).
3. Courtillot V.*, et al.* Deccan flood basalts and the Cretaceous/Tertiary boundary. *Nature*, **333**, 843-846 (1988).
4. Duncan R.A. & Hargraves R.B. 40Ar/39Ar Geochronology of basement rocks from the Mascarene plateau, the Chagos bank and the Maldives ridge. *Proc. Ocean Drill. Program, Sci. Results*, vol. 115, pp 43-51 (1990).

5. Montelli R., Nolet G., Dahlen F.A. & Masters G. A catalogue of deep mantle plumes: New results from finite-frequency tomography. *Geochem. Geophys. Geosyst.*, **7**, Q11007 (2006).

6. French S.W. & Romanovicz B. Broad plumes rooted at the base of the Earth's mantle beneath major hotspots. *Nature*, **525**, 95-101 (2015).

7. Ritsema J. Evidence for shear velocity anisotropy in the lowermost mantle beneath the Indian Ocean. *Geophys. Res. Lett.*, **27**, 1041-1044 (2000).

8. Morgan W.J. Rodriguez, Darwin, Amsterdam,..., a second type of hotspot island. *J. Geophys. Res.*, **83**, 5357-5360 (1978).

9. Duncan R.A. The volcanic record of the Réunion hotspot. *Proc. Ocean Drill. Program, Sci. Results*, vol. 115, pp 3-10 (1990).

10. Dyment J., Lin J. & Baker E.T. Ridge-hotspot interactions: What Mid-Ocean Ridges Tell Us About Deep Earth Processes. *Oceanography*, **20**, 102-115 (2007).

11. McDougall I., Upton B.G.J. & Wadsworth W.J. A geological reconnaissance of Rodriguez Island Indian Ocean. *Nature*, **206**, 26-27 (1965).

12. Mahoney J.J.*, et al.* Isotopic and geochemical provinces of the western Indian Ocean Spreading Centers. *J. Geophys. Res.*, **94**, 4033-4052 (1989).

13. Nauret F.*, et al.* Correlated trace element-Pb isotope enrichments in Indian MORB along 18-20 circle S, Central Indian Ridge. *Earth Planet. Sci. Lett.*, **245**, 137-152 (2006).

14. Füri E.*, et al.* Helium isotope variations between Reunion Island and the Central Indian Ridge (17 degrees-21 degrees S): New evidence for ridge-hot spot interaction. *J. Geophys. Res.*, **116**, (2011).

15. Murton B.J., Tindle A.G., Milton J.A. & Sauter D. Heterogeneity in southern Central Indian Ridge MORB: Implications for ridge–hot spot interaction. *Geochem. Geophys. Geosyst*, **6**, Q03E20 (2005).

16. Okal E.A. & Stewart L.M. Slow earthquakes along oceanic fracture zones: evidence for asthenospheric flow away from hotspots? *Earth Planet. Sci. Lett.*, **57**, 75-87 (1982).
17. Barruol G. & Sigloch K. Investigating La Réunion Hot Spot From Crust to Core. *EOS Trans. Am. Geophys. Union*, **94**, 205-207 (2013).
18. Mazzullo A.*, et al.* Anisotropic Tomography around La Réunion Island from Rayleigh Waves. *J. Geophys. Res.*, **122**, 1-17 (2017).
19. Scholz J.-R.*, et al.* SKS splitting in the Western Indian Ocean from land and seafloor seismometers: Plume, Plate and Ridge signatures. *Earth Planet. Sci. Lett.*, **498**, 169-184 (2018).
20. Seton M.*, et al.* Global continental and ocean basin reconstructions since 200Ma. *Earth-Science Reviews*, **113**, 212-270 (2012).
21. Stixrude L. & Lithgow-Bertelloni C. Mineralogy and elasticity of the oceanic upper mantle: Origin of the low-velocity zone. *J. Geophys. Res.*, **110**, B03204 (2005).
22. Debayle E. & Lévêque J.J. Upper mantle heterogeneities in the Indian Ocean from waveform inversion. *Geophys. Res. Lett.*, **24**, 245-248 (1997).
23. Ma Z. & Dalton C.A. Evolution of the lithosphere in the Indian Ocean from combined earthquake and ambient noise tomography. *J. Geophys. Res.*, **122**, 354-371 (2017).
24. Nicolas A. & Christensen N.I. Formation of anisotropy in upper mantle peridotites-A review. In: Fuchs K, Froidevaux C (eds). *Composition, Structure and Dynamics of the Lithosphere-Asthenosphere System*, vol. 16. AGU: Washington, D. C., pp 111-123 (1987).
25. Mainprice D., Barruol G. & Ben Ismail W. The seismic anisotropy of the Earth's mantle: from single crystal to polycrystal. In: Karato SI, Forte A, Liebermann RC, Masters G, Stixrude L (eds). *Earth's deep interior: Mineral Physics and*

Tomography from the atomic to the global scale, vol. 117. AGU: Washington, D.C., pp 237-264 (2000).

26. Barruol G. & Fontaine F.R. Mantle flow beneath La Réunion hotspot track from SKS splitting. *Earth Planet. Sci. Lett.*, **362**, 108-121 (2013).

27. Stotz I.L., Iaffaldano G. & Davies D.R. Pressure-Driven Poiseuille Flow: A Major Component of the Torque-Balance Governing Pacific Plate Motion. *Geophys. Res. Lett.*, **45**, 117-125 (2018).

28. Natarov S.I. & Conrad C.P. The role of Poiseuille flow in creating depth-variation of asthenospheric shear. *Geophys. J. Int.*, **190**, 1297-1310 (2012).

29. Lin P.-Y.P.*, et al.* High-resolution seismic constraints on flow dynamics in the oceanic asthenosphere. *Nature*, **535**, 538-541 (2016).

30. Becker T.W. & Faccenna C. Mantle conveyor beneath the Tethyan collisional belt. *Earth Planet. Sci. Lett.*, **310**, 453-461 (2011).

31. Forte A.*, et al.* Joint seismic-geodynamic-mineral physical modelling of African geodynamics: a reconciliation of deep-mantle convection with surface geophysical constraints. *Earth Planet. Sci. Lett.*, **295**, 329-341 (2010).

32. Morgan W.J. & Morgan J.P. Plate velocities in the hotspot reference frame. In: Foulger GR, Jurdy DM (eds). *Plates, plumes, and planetary processes*, vol. 430. Geological Society of America Special Paper, pp 65-78 (2007).

33. Argus D.F., Gordon R.G. & DeMets C. Geologically current motion of 56 plates relative to the no-net-rotation reference frame. *Geochem. Geophys. Geosyst*, **12**, Q11001 (2011).

34. Kim J., Pak S.-J., Moon J.-W., Lee S.-M. & Stuart F.M. Mantle heterogeneity in the source region of mid-ocean ridge basalts along the northern Central Indian Ridge (8°S–17°S). *Geochem. Geophys. Geosyst.*, **18**, 1419–1434 (2017).

35. Hable S., Sigloch K., Stutzmann E., Kiselev S. & Barruol G. Tomography of crust and lithosphere in the western Indian Ocean from noise cross-correlations of land and ocean bottom seismometers. *Geophys. J. Int.*, **219**, 924-944 (2019).

36. Ito G., Lin J. & Gable C.W. Interaction of mantle plumes and migrating mid-ocean ridges: Implications for the Galapagos plume-ridge system. *J. Geophys. Res*, **102**, 15403-15417 (1997).

37. Mittal T. & Richards M.A. Plume-ridge interaction via melt channelization at Galápagos and other near-ridge hotspot provinces. *Geochem. Geophys. Geosyst.*, **18**, 1711-1738 (2017).

38. Maia M.*, et al.* Building of the Amsterdam-Saint Paul plateau: A 10 Myr history of a ridge-hot spot interaction and variations in the strength of the hot spot source. *J. Geophys. Res.*, **116**, (2011).

39. Iaffaldano G., Davies D.R. & DeMets C. Indian Ocean floor deformation induced by the Reunion plume rather than the Tibetan Plateau. *Nature Geosci.*, **11**, 362-366 (2018).

40. Kumagai I., Davaille A., Kurita K. & Stutzmann E. Mantle plumes: Thin, fat, successful, or failing? Constraints to explain hot spot volcanism through time and space. *Geophys. Res. Lett.*, **35**, (2008).

41. Debayle E. & Ricard Y. Seismic observations of large-scale deformation at the bottom of fast-moving plates. *Earth Planet. Sci. Lett.*, **376**, 165-177 (2013).

42. Tsekhmistrenko M., Sigloch K. & Hosseini K. Whole-mantle structure under the Reunion hotspot in the western Indian Ocean from multifrequency P-wave tomography. EGU; 2018; Vienna; 2018. p. EGU2018-1076.

43. Sleep N.H. Channeling at the base of the lithosphere during the lateral flow of plume material beneath flow line hot spots. *Geochem. Geophys. Geosyst.*, **9**, Q08005 (2008).

44. French S., Lekic V. & Romanovicz B. Waveform tomography reveals channeled flow at the base of the oceanic asthenosphere. *Science*, **342**, 227-230 (2013).

45. Montagner J.P. Upper mantle low anisotropy channels below the Pacific plate. *Earth Planet. Sci. Lett.*, **202**, 263-274 (2002).

46. O'Connor J., Jokat W., Wijbrans J. & Colli L. Hotspot tracks in the South Atlantic located above bands of fast flowing asthenosphere driven by waning pulsations from the African LLSVP. *Gondwana Research*, **53**, 197-208 (2018).

47. Yamamoto M., Morgan J.P. & Morgan W.J. Global plume-fed asthenosphere flow—II: Application to the geochemical segmentation of mid-ocean ridges. In: Foulger GR, Jurdy DM (eds). *Plates, plumes, and planetary processes*, vol. 430: Geological society of America Special Paper, pp 189-208 (2007).

48. Morgan J.P., Morgan W.J., Zhang Y.S. & Smith W.H.F. Observational hints for a plume-fed, suboceanic asthenosphere and its role in mantle convection. *J. Geophys. Res.*, **100**, 12753-12767 (1995).

49. Fontaine F.R.*, et al.* Crustal and Uppermost Mantle structure variation beneath La Réunion hotspot track. *Geophys. J. Int.*, **203**, 107-126 (2015).

Corresponding author:

Guilhem Barruol, Institut de physique du globe de Paris, France, barruol@ipgp.fr

Acknowledgements

RHUM-RUM was funded by the Agence Nationale de la Recherche in France (project ANR-11-BS56-0013) and by the Deutsche Forschungsgemeinschaft in Germany (grants SI1538/2-1 and SI1538/4-1), with additional supports from Centre

National de la Recherche Scientifique – Institut National des Sciences de l'Univers (CNRS-INSU), Terres Australes et Antarctiques Françaises (TAAF), Institut Polaire Paul Emile Victor (IPEV), Université de La Réunion and Alfred Wegener Institut (AWI). OBS were provided by DEPAS (Deutsche Geräte-Pool für Amphibische Seismologie, Germany), GEOMAR (GEOMAR Helmholtz-Zentrum für Ozeanforschung Kiel, Germany) and INSU-IPGP (Institut National des Sciences de l'Univers - Institut de Physique du Globe de Paris, France). K.S. was funded by Deutsche Forschungsgemeinschaft grants SI1538/2-1 and SI1538/4-1, and by the People Programme (Marie Curie Actions) of the European Union's Seventh Framework Programme FP7/2007-2013/ under REA grant agreement no PCIG14-GA-2013-631104 "RHUM-RUM''. JPM was funded by IUF (Institut Universitaire de France). Thanks to the crews of cruises *Marion Dufresne 192* and *Meteor 101* and to TIDES Cost Action for organizing meetings and discussions. We thank Michael Wysession for sharing MACOMO data, Céline Davy and Eric Delcher for their field and instrumental help. This is IPGP contribution 4068.

Author contributions

G.B., K.S., J.-R.S., A.M., E.S., S.K., F.R.F and J.-P.M. performed the analysis of the data, G.B. and K.S. were in charge of data acquisition and pre-processing, and led the writing of the manuscript. All authors participated in interpreting the results.

Financial and non-financial competing interests

The authors declare no competing financial interests.

Figure Captions

Figure 1: Seismological imaging of the Rodrigues Corridor region, from Réunion to the Central Indian Ridge (CIR). a) Bathymetric map showing SKS splitting measurements[19,26] (black bars) at RHUM-RUM ocean-bottom and island stations (yellow dots). Bar lengths and azimuths represent magnitudes and fast directions of SKS splitting. Grey dashed lines are seafloor age isochrons up to 40 million years. b-f) Shear-wave velocity variations *dVs/Vs* (red=slow, blue=fast) from Rayleigh-wave tomography[18] at depths of 50, 60, 70, 80 and 90 km. Thick dashed and thin dotted lines are isocontours of *dVs/Vs* = ±2% and ±1%, respectively. Black bars are azimuthal anisotropy estimates from tomography, normalized as shown beneath the colour bar.

Figure 2: Surface-wave tomography[18] of the western Indian Ocean. a) Bathymetric map showing RHUM-RUM OBS locations (yellow dots) and spreading ridges: South West Indian Ridge (SWIR), South East Indian Ridge (SEIR), Central Indian Ridge (CIR), Carlsberg Ridge (CR) and Rodrigues Triple Junction (RTJ). b-f) Shear wave velocity variations *dVs/Vs* at depths of 50, 80, 120, 170 and 200 km, shown on the same (logarithmic) colour scale as in Fig. 1. Black bars show azimuthal anisotropy estimates from tomography as in Fig. 1.

Figure 3: Shape and dynamics of the Mascarene Basin Asthenospheric Reservoir (MBAR): a) Map of lithosphere thickness or LAB depth (blue shades), estimated from surface-wave tomography[21] as depth of the 1200°C isotherm. Blue shades inside black circles are independent LAB depth estimates under Réunion, Mauritius and Rodrigues islands from receiver function and surface-wave dispersion data[49]. Orange bars show azimuthal anisotropy in the lithosphere at 50 km depth. b): Three-dimensional rendering of anomalously slow asthenosphere (-*dVs/Vs*>1.5%

slow isocontour), at and below 100 km depth. The depth axis is reversed as if mantle structure were turned inside-out (light pink is deep, red is shallower). Yellow bars show anisotropy 50 km below the LAB, where asthenospheric anomalies tend to peak. Dashed blue lines indicate cross sections presented in Fig. 4.

Figure 4: Upper mantle structure and Poiseuille-like asthenospheric flow beneath the Western Indian Ocean. East-west cross-sections through the MBAR (7.5°S, 12.5°S), Rodrigues corridor (18.5°S), and south (21.5°S, 26.5°S) of those two bodies of very slow asthenosphere. Isotropic *dVs/Vs* is represented by the same colour scale as in Figs. 1 and 2. Azimuthal anisotropy is shown by black bars, in 10-km vertical increments. Horizontal and vertical bars indicate east-west and north-south striking directions, respectively. Magnitude is normalized as in the legend. Green circles and red stars mark the longitudes of the CIR and Réunion island, respectively. Green dashed lines indicate the "1200°C isotherm" LAB estimates[21] shown in Fig. 3a.

Figure 5: Conceptual summary of shallow and deep flows in the asthenosphere beneath the western Indian Ocean. Block diagram (roughly to scale) shows the shallow asthenospheric channel under the Rodrigues corridor, from Réunion towards the CIR, and its eastward, Poiseuille-type flow velocity profile that aligns the olivine [100] fast axes east-west. Red dots are OBS locations, black bars are SKS splitting measurements. Lower map shows isotropic and anisotropic S-velocities at 140 km depth, where the dotted black rectangle indicates the extent of the block diagram. Grey interpretive arrows highlight the shallow, hotspot-to-CIR flow in the Rodrigues corridor asthenosphere, and the deeper, broader flows within MBAR asthenosphere, towards and beyond the CIR.

Methods

Seismological networks. The RHUM-RUM experiment[17] deployed 57 ocean-bottom seismometers (OBS, shown as triangles in Supplementary Figure S1) in October 2012 with the French research vessel *Marion Dufresne* (cruise MD192[50]), and recovered them in December 2013 with the German *Meteor* (cruise M101[51]). Over half of the OBS were deployed over the "Rodrigues corridor", stretching from Réunion to the CIR via Mauritius and Rodrigues (Fig. 2a and Supplementary Fig. S1). The OBS measured continuous ground motion (velocity) along one vertical and two horizontal components. The network consisted of 9 stations equipped with Nanometrics Trillium 240s broadband sensors (red triangles in Fig. S1), loaned from the French INSU-IPGP pool (Institut National des Sciences de l'Univers - Institut de Physique du Globe de Paris), and of 48 stations equipped with Guralp 60s or 120s wideband sensors (yellow triangles in Fig. S1), from the German DEPAS pool (Deutsche Geräte-Pool für amphibische Seismologie) managed by Alfred Wegener Institut Bremerhaven. Technical details on the experiment and data pre-processing have been published[52-54].

RHUM-RUM also deployed 20 terrestrial stations on Réunion (10), the Îles Éparses and Mayotte in the Mozambique Channel (5), and South-East Madagascar (5) (white diamonds in Fig. S1). For our SKS studies we further used permanent island station MRIV on Mauritius (operated by Mauritius Meteorological Services), and stations RER (on Réunion) and RODM (on Rodrigues), operated by the GEOSCOPE network (doi:10.18715/*GEOSCOPE*.G). 33 stations from the MACOMO experiment[55,56], installed between 2011-2013 in Madagascar (Fig. S1), were also integrated in the surface wave tomography analysis[18].

548 **Surface wave tomography.** For our Rayleigh wave tomography[18] we used ~300
549 regional and teleseismic earthquakes with high signal-to-noise ratios recorded at
550 ocean-bottom, island and land stations across the Western Indian Ocean that
551 allowed to invert 9000 phase-velocity measurements of fundamental-mode Rayleigh
552 waves (30s-300s period) for isotropic *dVs/Vs*, which is primarily a proxy for mantle
553 temperature, and for azimuthally anisotropic *dVs/Vs*, a proxy for current or past
554 mantle flow.
555 For each earthquake-station path, we measured phase velocities of fundamental-
556 mode Rayleigh waves in the period range of 30-300s using the "roller-coaster"
557 method[57], and group velocities in the period range of 16-250s using time-frequency
558 analysis. A three-dimensional (3-D) model of shear wave velocity in the upper mantle
559 was obtained as follows. First, we inverted the path-averaged phase and group
560 velocities to obtain regionalized velocity maps for each period separately. Second,
561 we combined all phase and group velocity maps corresponding to different periods
562 and inverted them at each grid point to obtain the local *S*-wave velocity as a function
563 of depth using a trans-dimensional inversion scheme. Third, these local models were
564 recombined to obtain the 3-D *S*-wave velocity and azimuthal anisotropy model with a
565 lateral resolution of 300 km down to depths of 350 km depth[18]. Radial anisotropy
566 could not be constrained as it would have required Love-wave measurements, which
567 are difficult to obtain from the particularly noisy horizontal components of OBS.
568
569 **Synthetic tests of the surface-wave tomography model: lateral resolution.** We
570 present two inversions of synthetic data aimed at testing the reliability and lateral
571 resolution of the velocity regionalization. Figure S2 presents a generic checkerboard
572 test, and Fig. S3 tests the robustness of an asthenospheric channel present in the
573 actual inversion. Additional tests can be found in Mazzullo et al. (2017)[18]. Path

density and azimuthal coverage of the tests are identical to those used in the inversion of the real data (Fig. S1).

The checkerboard test input (here, for phase velocities, period 100 s) consists of 500 km wide, vertical parallelepipeds of alternating slow and fast velocities (Fig. S2a), which also include azimuthal anisotropy with fast directions trending perpendicular from one block to the next (Fig. S2c). Recovery is good for both isotropic (Fig. S2b) and anisotropic (Fig. S2d) structures, especially in the Western Indian Ocean centered on the Réunion-Rodrigues and MBAR areas.

In Supplementary Fig. S3a, the resolution test input (here, for phase velocities, period 80 s) consists of a negative velocity anomaly modelled on a low-velocity channel under the Rodrigues corridor between Réunion island and the CIR. We consider a 1000 km long and 200 km wide parallelepiped with an (isotropic) velocity anomaly of *dVs/Vs* = -3% relative to the reference model (Supplementary Fig. S3a). Recovery of the overall structure is good (Fig. S3b), with very little smearing in N-S direction (the narrower dimension), and moderate smearing of ~200 km in E-W direction.

Synthetic tests of the surface-wave tomography model: vertical resolution of azimuthal anisotropy. We performed inversions of synthetic data in order to check the vertical resolution of the surface-wave tomography model, specifically its ability to constrain azimuthal anisotropy as a function of depth. Anisotropy is caused by differential movement in the rock matrix (shear strain). In the case of horizontal flow, strain is due to differing horizontal flow velocities as a function of depth within the flowing layer (asthenosphere), i.e., strain is a function of *dVh/dz*, where *Vh* is horizontal fluid velocity, and *z* is depth below the LAB. Supplementary Fig. S4 schematically compares the vertical profiles of fluid flow, shear, and anisotropy in the asthenosphere, for the cases of Couette and Poiseuille flows.

In the Couette flow case (Supplementary Fig. S4a), asthenosphere is dragged by the overlying lithosphere. Strain and azimuthal anisotropy are expected to peak at the LAB (where *Vh* decreases most rapidly with depth), and to decrease with depth, a pattern suggested by numerical models[58]. In the case of Poiseuille flow (Fig. S4b & c), lithosphere and asthenosphere are decoupled, and horizontal flow is driven by a horizontal pressure gradient (which is constant as a function of depth). In an iso-viscous asthenosphere (Fig. S4b), one expects a parabolic flow pattern as a function of depth, which results in minimum shear and anisotropy in the middle of the asthenosphere[28,29] and local maxima on either side of the minimum, leading to a "two-spindle" anisotropy profile unlike the "one-spindle" profile we actually observe in MBAR asthenosphere. In the non-linear, strongly temperature-dependent rheology of mantle rocks, the asthenosphere is likely to have internal viscosity variations and to be softest in the middle, where isotropic *dVs/Vs* (a proxy for temperature and/or water content) is observed to peak. The resulting Poiseuille flow (Fig. S4c) concentrates shear in the weakest zone and predicts the one-spindle anisotropy profile observed in the MBAR.

Our resolution tests presented in Fig. S5 are aimed at testing whether the one-spindle profile of Fig. S4c is resolvable given our tomographic data coverage, and whether the dominance of plate drag (Couette profile of Fig. S4a) can be ruled out.

In both Couette and Poiseuille cases, we considered a homogeneous, 80 km-thick lithosphere above a 120-km thick, flowing asthenosphere (depth 80-200 km), underlain by a mesosphere halfspace, which does not move nor deform. The lithosphere features 2% anisotropy with a fast direction of N030°E, which is modelled on the "frozen in" anisotropy observed for Mascarene Basin lithosphere (Figs. 2b, 3a and 4) and conforms to the paleo-spreading direction.

For the Couette flow test, the dragging Somali lithosphere is modelled to move N075°E (Fig. S5a), inducing an asthenospheric anisotropy of the same strike

(N075°E), at an angle of 45° from the lithospheric anisotropy (Fig. S5b, red line). Asthenospheric anisotropy is considered to reach its peak of 3% at the LAB, gradually decreasing to 0% at 200 km depth (Fig. S5c, red line).

In the case of (non-isoviscous) Poiseuille flow (Fig. S4c, S5d), lithospheric motion has no influence on asthenospheric anisotropy since the two layers are decoupled. We model asthenospheric anisotropy to strike N060°W (Fig. S5e, red line), as observed for the asthenosphere of the MBAR, with a maximum amplitude of 3% in the middle of the layer (125 km depth) and zero amplitude at its top and bottom (Fig. S5f, red line).

S-wave velocity is parametrized[59] as

$$Vs = \sqrt{\frac{(L+Gc\cos 2\psi+Gs\sin 2\psi)}{\rho}}$$

and the anisotropy parameters inverted for are *L*, *Gc* and *Gs* as a function of depth. The percentage of anisotropy is $A = 100\%\frac{\sqrt{(Gc^2+Gs^2)}}{L}$ and the anisotropy azimuth is $\psi = \mathrm{atan}\left(\frac{Gs}{Gc}\right)$. For details on the inversion scheme, see section (4) in Mazzullo et al.[18].

The resolution test results are plotted as blue dotted lines in Fig. S5, panels b, c, e, and f. Although imperfect data coverage and wave sensitivities have a smoothing effect on the recovered vertical profiles, the azimuths and amplitudes of anisotropy are retrieved in both models. The magnitude of anisotropy appears to be a robust discriminating factor between the two competing models.

In the Couette flow case, the test faithfully recovers the high amplitude of anisotropy at the LAB (Fig. S5c, blue dashed), a result that is clearly distinguishable from the zero crossings observed for the MBAR and recovered to good approximation by the Poiseuille-case test (see below). Regarding directions, the input of a 45 degrees jump of anisotropy azimuth across the LAB in Fig. S5b is recovered as a gradual

653 rotation from lithospheric to asthenospheric strike, over a depth range from ~30 km
654 above the LAB to ~30 km below it.
655 In the Poiseuille flow case, the test robustly resolves a pronounced minimum of
656 anisotropy amplitude at the LAB, almost matching the input of zero (Supplementary
657 Fig. S5f, blue versus red). This result is robustly distinguishable from the Couette
658 flow test (Supplementary Fig. S5c, blue), and is consistent with our MBAR
659 observations. The spindle-shaped input pattern for the asthenosphere is well
660 recovered. The jump of anisotropy azimuths across the LAB (Fig. S5e, red) is
661 smoothed over a smaller vertical range (blue) than in the Couette test (Fig. S5b,
662 blue), consistent with what is observed.
663 The Couette flow scenario makes a clear prediction for the asthenospheric direction
664 of anisotropy (NE-ward), and this prediction is clearly distinct from the observed
665 MBAR direction (SE-ward). Since anisotropy directions are very accurately recovered
666 by the tests, our observations provide strong evidence against dominance of Couette
667 flow.
668 The tests suggest that the observed absence (or "zero-crossing") of anisotropy at the
669 LAB is a real feature, as are the spindle-shaped anisotropy profiles observed in the
670 asthenosphere in main Fig. 4. This supports the dominance of Poiseuille-like flow in
671 the Mascarene Basin asthenosphere, implying that lithosphere and asthenosphere
672 are largely decoupled in this region.
673 Across the asthenosphere-mesosphere boundary, azimuths are recovered very
674 accurately, and if one had to pick the asthenosphere-mesosphere boundary from the
675 vertical profile of anisotropy magnitude, the result would not differ much whether it
676 was done on the test input or output curves. This supports our claim that the lower
677 ends of the anisotropy spindles observed in main Fig. 4 should be good estimates for
678 the depth of the asthenosphere-mesosphere boundary, the lower limit of the flowing
679 layer.

680

681 **Tomography-based estimates of lithospheric thickness (LAB depth).** We
682 estimated lithospheric thickness in the western Indian Ocean (in blue shades main
683 Fig. 3a) using two different approaches, both based on isotropic shear wave
684 velocities *Vs0* obtained from surface wave tomography[18].
685 (1) LAB depth equals the depth where the minimum (i.e., the largest negative value)
686 of the vertical gradient in *Vs0* is located[60], or visually speaking, the most rapid vertical
687 transition from blue to red on the tomographic colour scale of Supplementary Fig. S6.
688 (2) LAB depth equals the depth of the 1200°C isotherm (or alternatively 1100°C or
689 1300°C isotherm), which is determined by an empirical formula relating isotropic
690 shear wave velocities to rock temperature according to Stixrude and Lithgow-
691 Bertelloni[21].
692 To avoid unrealistic lateral jumps for either approach, we smoothed the resulting
693 lithospheric thickness for each map point, by averaging over its eight closest
694 neighbours, i.e., over a radius of ~150 km.
695 The LAB depth estimates obtained from these methods are compared in
696 Supplementary Fig. S6 (green lines) on an EW tomography cross-section located at
697 10.5°S. There is good agreement between the two methods, in particular beneath the
698 Mascarene Basin and the CIR, and hence we show only the 1200°C LAB estimate in
699 the cross-sections of main Fig. 4. The same 1200°C LAB estimates (laterally
700 smoothed) are shown in the lithospheric thickness map of main Fig. 3a. Our
701 tomography-derived LAB depth values are independently confirmed beneath islands
702 by, and in good agreement with, depths obtained from joint inversion of receiver
703 function and surface wave dispersion data, which used permanent island stations[49].
704 They found LAB depths of ≈70 km beneath Réunion, ≈50 km beneath Mauritius, and
705 ≈25 km beneath Rodrigues (shown in main Fig. 3a as circles filled with appropriate
706 blue shades). The close focusing of the various LAB suggests a rather strong

temperature gradient and therefore a sharp lithosphere-asthenosphere transition, as also observed in the NW Pacific Ocean[61,62]. Since alternative LAB solutions cluster quite closely, we chose to show only the 1200°C LAB estimate in the cross-sections of Fig. 4, for the sake of readability.

Empirically, we find that asthenospheric anisotropy and negative isotropic *dVs/Vs* both tend to peak ~50 km beneath the "1200°C LAB". For a representative summary of asthenospheric flow (in main Fig. 3b), we therefore extracted tomographic anisotropy values along an undulating hypersurface running 50 km beneath the 1200°C LAB (white dashed lines in Fig. S6).

Reconciling tomography and shear-wave splitting results. Observations of the splitting of SKS waves have been used to scan continents[63-65] and more recently the oceans[66-68] for (upper mantle) seismic anisotropy, which is accepted to result from crystal-preferred orientations of the rock-forming minerals[24,25].

Prior to the RHUM-RUM experiment, SKS splitting measurements in the western Indian Ocean were limited to Madagascar[56,69] and the islands of Réunion[26,70,71], Mauritius, Seychelles[72] and Rodrigues[26]. To analyse the RHUM-RUM data[19], we used teleseismic earthquakes of $Mw \geq 5.8$ at epicentral distances ranging from 85°–130° and measured the fast polarization axis (ϕ) and splitting delay time (δt) using the *SplitLab* software[73]. Measurements were performed using the eigenvalue approach[63], after carefully correcting for horizontal sensor orientations of the ocean-bottom seismometers[53].

Reconciling anisotropy observations from body and surface waves has been challenging for a long time[74-76] and is not a primary purpose of this paper. Lateral resolution of SKS splitting measurements is ~50 km at 100 km depth, whereas our surface wave tomography provides lateral resolution of ~300 km. An apparent observational contradiction likely resulting from these different sensitivities concerns

734 the Rodrigues corridor. SKS splits along the corridor (Fig. 1a) indicate strong, E-W
735 striking fast directions, whereas surface-wave anisotropy is relatively weak and
736 diffuse in this region (Fig. 2d and 3b). SKS results are expected to be very robust
737 because individual measurements are independent (station spacing is larger than the
738 measurement sensitivity zone of ~50 km) and consistently yield the same, strong E-
739 W directions. Moreover, tomography sees the same strong E-W anisotropy just
740 slightly further north in the MBAR. At face value, surface wave anisotropy is at odds
741 with the SKS splits, but taken together, this leaves the explanation that anisotropy in
742 the Rodrigues corridor is strong and consistently aligned (in fact similar to what
743 tomography finds in the larger-scale MBAR further north), but that the relatively small
744 corridor (~1000 km x 400 km) seems to be sharply bounded by structure that is very
745 different, especially to the south, which destroys any MBAR-like clarity in the surface-
746 wave (resolution lengths ~300-km) averaging over structures inside and outside the
747 corridor.
748
749 **Predicting SKS splitting parameters from the anisotropic surface wave model.**
750 The quantity and quality of our SKS measurements was not sufficient to infer the
751 respective splitting contributions of lithosphere and asthenosphere separately.
752 Hence, we calculated theoretical SKS splitting parameters for these two layers from
753 our surface-wave tomography model. Surface-wave tomography confidently
754 constrains the vertical profiles of isotropic shear-velocity (*Vs0*) and anisotropic fast
755 split directions, but its lateral resolution of ~200-300 km is low compared to SKS
756 measurements (~50 km). This means that SKS splits forward-predicted through a
757 tomography model will differ from actual SKS observations, to the extent that earth
758 structure is heterogeneous on such length scales.
759 We use the Rayleigh-wave model's *n* anisotropic depth-layers[77] to forward-predict
760 the fast split directions and delay times acquired beneath each seismic station for

761 three simple cases: (1) only in the lithospheric layer (from 25 km depth to the LAB);
762 (2) only in the asthenospheric layer (LAB to 300 km depth); and (3) in the combined
763 lithosphere + asthenosphere package, i.e., 25 to 300 km depth).
764 SKS splitting predictions for only the lithosphere (Supplementary Fig. S7a, orange
765 bars) show clear N-S trending fast split directions throughout the area west of
766 Réunion and Mauritius, with delay times <0.3 s (i.e., small compared to the
767 observations, black bars). Magnitude of anisotropy is less robustly estimated by
768 tomography (typically underpredicted), which probably explains our persistent
769 underprediction of SKS splits. We attribute the N-S trending fast split pattern to the
770 identical paleo-spreading direction of the Mascarene Basin[19,20], which formed this
771 lithosphere between 60-80 Ma.
772 Between Mauritius and the Central Indian Ridge, predicted lithospheric split times are
773 even smaller, likely a combined effect of thinner lithosphere[49] towards the CIR and
774 lower amplitude of the frozen-in anisotropy.
775 For the asthenosphere (Fig. S7b), splitting predictions generally strike E-W,
776 especially close to the CIR, showing good directional agreement with observed fast
777 splits from SKS phases. At several stations between Réunion Island and Rodrigues
778 Ridge, the predicted fast split directions trend NE-SW. We attribute this to the
779 presence of slight singularities (undesired, non-smoothed artefacts) in the Rayleigh
780 wave model at depths >200 km (e.g. middle panel in Fig 4, at 60.5°E longitude),
781 which cause this rotation in the modelled directions. Importantly, between Réunion
782 and the CIR, we predict asthenospheric delay times as high as 1 s, much higher than
783 the predicted contribution of the overlying lithosphere (Fig. S7a). Assuming the same
784 ratio holds for the two layers' contributions to the actually observed SKS splits, this
785 result implies that ~80% of the observed SKS split times stem from the
786 asthenosphere, justifying their interpretation in terms of east-west directed
787 asthenospheric flow. In 100-150 km thick asthenosphere (Fig. 4 and 5), these

788 splitting magnitudes would be produced vertically from uniform 3-5% *Vs*-anisotropy[25],
789 or accordingly stronger anisotropy in the central maximum of a spindle profile. This
790 dominance of asthenospheric anisotropy is also visible in Fig. S7c, where the
791 combined lithosphere + asthenosphere predictions in the Rodrigues corridor look
792 very similar to those in Fig. S7b.
793

794 **References**

795 Cited in Main text

796

797 17. Barruol G. & Sigloch K. Investigating La Réunion Hot Spot From Crust to
798 Core. *EOS Trans. Am. Geophys. Union*, **94**, 205-207 (2013).
799 18. Mazzullo A.*, et al.* Anisotropic Tomography around La Réunion Island from
800 Rayleigh Waves. *J. Geophys. Res.*, **122**, 1-17 (2017).
801 19. Scholz J.-R.*, et al.* SKS splitting in the Western Indian Ocean from land and
802 seafloor seismometers: Plume, Plate and Ridge signatures. *Earth Planet. Sci.*
803 *Lett.*, **498**, 169-184 (2018).
804 20. Seton M.*, et al.* Global continental and ocean basin reconstructions since
805 200Ma. *Earth-Science Reviews*, **113**, 212-270 (2012).
806 21. Stixrude L. & Lithgow-Bertelloni C. Mineralogy and elasticity of the oceanic
807 upper mantle: Origin of the low-velocity zone. *J. Geophys. Res.*, **110**, B03204
808 (2005).
809 24. Nicolas A. & Christensen N.I. Formation of anisotropy in upper mantle
810 peridotites-A review. In: Fuchs K, Froidevaux C (eds). *Composition, Structure*
811 *and Dynamics of the Lithosphere-Asthenosphere System*, vol. 16. AGU:
812 Washington, D. C., pp 111-123 (1987).

25. Mainprice D., Barruol G. & Ben Ismail W. The seismic anisotropy of the Earth's mantle: from single crystal to polycrystal. In: Karato SI, Forte A, Liebermann RC, Masters G, Stixrude L (eds). *Earth's deep interior: Mineral Physics and Tomography from the atomic to the global scale*, vol. 117. AGU: Washington, D.C., pp 237-264 (2000).

26. Barruol G. & Fontaine F.R. Mantle flow beneath La Réunion hotspot track from SKS splitting. *Earth Planet. Sci. Lett.*, **362**, 108-121 (2013).

28. Natarov S.I. & Conrad C.P. The role of Poiseuille flow in creating depth-variation of asthenospheric shear. *Geophys. J. Int.*, **190**, 1297-1310 (2012).

29. Lin P.-Y.P.*, et al.* High-resolution seismic constraints on flow dynamics in the oceanic asthenosphere. *Nature*, **535**, 538-541 (2016).

49. Fontaine F.R.*, et al.* Crustal and Uppermost Mantle structure variation beneath La Réunion hotspot track. *Geophys. J. Int.*, **203**, 107-126 (2015).

References cited in Methods only

50. Barruol G. Cruise Report, R/V MARION DUFRESNE, cruise N°MD192, Sept - Oct 2012; doi:10.13140/2.1.2492.0640, 2013.

51. Sigloch K. Cruise Report R/V METEOR, Cruise No. 101: METEOR- Berichte: DFG- Senatskommission für Ozeanographie; doi:10.2312/cr_m101, 2014.

52. Stähler S.C.*, et al.* Performance report of the RHUM-RUM ocean bottom seismometer network around La Réunion, western Indian Ocean. *Adv. Geosci.*, **41**, 43-63 (2016).

53. Scholz J.-R.*, et al.* Orienting Ocean-Bottom Seismometers from P- and Rayleigh waves polarizations. *Geophys. J. Int.*, **208**, 1277-1289 (2017).

54. Hable S., Sigloch K., Barruol G., Stähler S.C. & Hadziioannou C. Clock errors in land and ocean bottom seismograms: High-accuracy estimates from

multiple-component noise cross-correlations. *Geophys. J. Int.*, **214**, 2014-2034 (2018).

55. Pratt M.J.*, et al.* Shear velocity structure of the crust and upper mantle of Madagascar derived from surface wave tomography. *Earth Planet. Sci. Lett.*, **458**, 405-417 (2017).

56. Ramirez C.*, et al.* Complex seismic anisotropy in Madagascar revealed by shear wave splitting measurements. *Geophys. J. Int.*, **215**, 1718-1727 (2018).

57. Beucler E., Stutzmann E. & Montagner J.P. Surface wave higher-mode phase velocity measurements using a roller-coaster-type algorithm. *Geophys. J. Int.*, **155**, 289-307 (2003).

58. Tommasi A. Forward modeling of the development of seismic anisotropy in the upper mantle. *Earth Planet. Sci. Lett.*, **160**, 1-13 (1998).

59. Montagner J.P. & Nataf H.C. A simple method for inverting the azimuthal anisotropy of surface-waves. *J. Geophys. Res.*, **91**, 511-520 (1986).

60. Burgos G.*, et al.* Oceanic lithosphere-asthenosphere boundary from surface wave dispersion data. *J. Geophys. Res.*, **119**, 1079-1093 (2014).

61. Kawakatsu H.*, et al.* Seismic evidence of sharp lithosphere-asthenosphere boundaries of oceanic plates. *Science*, **324**, 499-502 (2009).

62. Kawakatsu H. & Utada H. Seismic and electrical signatures of the lithosphere–asthenosphere system of the normal oceanic mantle. *Ann. Rev. Earth Planet. Sci.*, **45**, 139-167 (2017).

63. Silver P.G. & Chan W.W. Shear wave splitting and subcontinental mantle deformation. *J. Geophys. Res.*, **96**, 16429-16454 (1991).

64. Silver P.G. Seismic anisotropy beneath the continents: Probing the depths of geology. *Ann. Rev. Earth Planet. Sci.*, **24**, 385-432 (1996).

65. Vinnik L.P., Farra V. & Romanovicz B. Azimuthal anisotropy in the earth from observations of *SKS* at Geoscope and NARS broadband stations. *Bull. Seismol. Soc. Amer.*, **79**, 1542-1558 (1989).

66. Barruol G.*, et al.* Mapping Upper Mantle flow Beneath French Polynesia from broadband ocean bottom seismic observations. *Geophys. Res. Lett.*, **36**, (2009).

67. Martin-Short R., Allen R.M., Bastow I.D., Totten E. & Richards M.A. Mantle flow geometry from ridge to trench beneath the Gorda–Juan de Fuca plate system. *Nature Geosci.*, **8**, 965-969 (2015).

68. Takeo A.*, et al.* Seismic azimuthal anisotropy in the oceanic lithosphere and asthenosphere from broadband surface wave analysis of OBS array records at 60 Ma seafloor. *J. Geophys. Res.*, **121**, 1927–1947 (2016).

69. Reiss M.C.*, et al.* Seismic anisotropy of the lithosphere and asthenosphere beneath southern Madagascar from teleseismic shear wave splitting analysis and waveform modeling. *J. Geophys. Res.*, **121**, 6627-6643 (2016).

70. Barruol G. & Ben Ismail W. Upper mantle anisotropy beneath the African IRIS and Geoscope stations. *Geophys. J. Int.*, **146**, 549-561 (2001).

71. Behn M.D., Conrad C.P. & Silver P.G. Detection of upper mantle flow associated with the African Superplume. *Earth Planet. Sci. Lett.*, **224**, 259-274 (2004).

72. Hammond J.O.S.*, et al.* Upper mantle anisotropy beneath the Seychelles microcontinent. *J. Geophys. Res.*, **110**, (2005).

73. Wuestefeld A., Bokelmann G.H.R., Zaroli C. & Barruol G. SplitLab: A shear-wave splitting environment in Matlab. *Computer & Geosciences*, **34**, 515-528 (2008).

74. Griot D.A., Montagner J.P. & Tapponnier P. Confrontation of mantle seismic anisotropy with two extreme models of strain in Asia. *Geophys. Res. Lett.*, **25**, 1447-1450 (1998).

75. Wuestefeld A., Bokelmann G.H.R., Barruol G. & Montagner J.P. Identifying global seismic anisotropy patterns by correlating shear-wave splitting and surface-wave data. *Phys. Earth Planet. Int.*, **176**, 198-212 (2009).

76. Becker T.W., Lebedev S. & Long M.D. On the relationship between azimuthal anisotropy from shear waves splitting and tomographic models. *J. Geophys. Res.*, **117**, (2012).

77. Silver P.G. & Savage M.K. The interpretation of shear-wave splitting parameters in the presence of two anisotropic layers. *Geophys. J. Int.*, **119**, 949-963 (1994).

Data sources

The RHUM-RUM data set (http://dx.doi.org/10.15778/RESIF.YV2011) has been assigned the FDSN network code YV and is hosted and freely accessible at the French RESIF data centre (http://seismology.resif.fr). MACOMO data are archived at the IRIS DMC (http://www.iris.edu) under the FDSN network code XV (https://doi.org/10.7914/SN/XV_2011). The individual RHUM-RUM SKS splitting measurements presented in this paper can be found online in the SKS splitting data base https://doi.org/10.18715/sks_splitting_database and mirrored and accessible at IRIS (Incorporated Research Institutions for Seismology) at https://ds.iris.edu/spud/swsmeasurement. We acknowledge the GEOSCOPE network (https://doi.org/10.18715/GEOSCOPE.G) for installing and maintaining permanent stations in the Indian Ocean.

Data availability

The authors declare that data supporting the findings of this study are freely available from RESIF data centre (http://seismology.resif.fr, http://dx.doi.org/10.15778/RESIF.YV2011).

Code availability

The shear wave splitting measurements were performed with the MATLAB-based *SplitLab* code available at https://github.com/IPGP/splitlab. The surface-wave tomography codes are not available on-line because tailored for laboratory work, but they can be requested by email to E.S. or S.K.

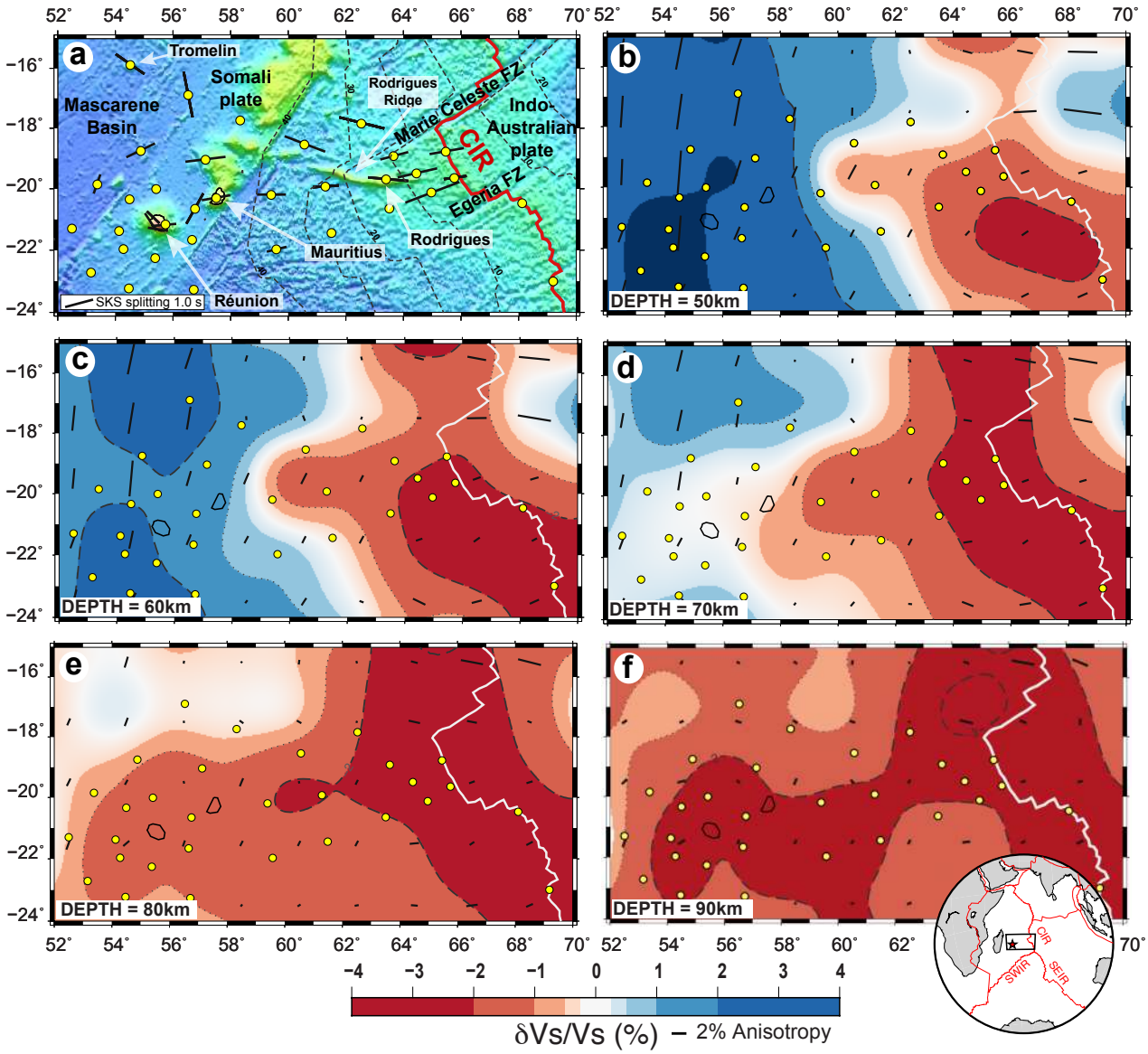

a
Tromelin
Somali plate
Mascarene Basin
Rodrigues Ridge
Marie Celeste FZ
CIR
Indo-Australian plate
Egeria FZ
Rodrigues
Mauritius
Réunion
SKS splitting 1.0 s
b
DEPTH = 50km
c
DEPTH = 60km
d
DEPTH = 70km
e
DEPTH = 80km
f
DEPTH = 90km
SWIR
SEIR
δVs/Vs (%) – 2% Anisotropy

Figure 1

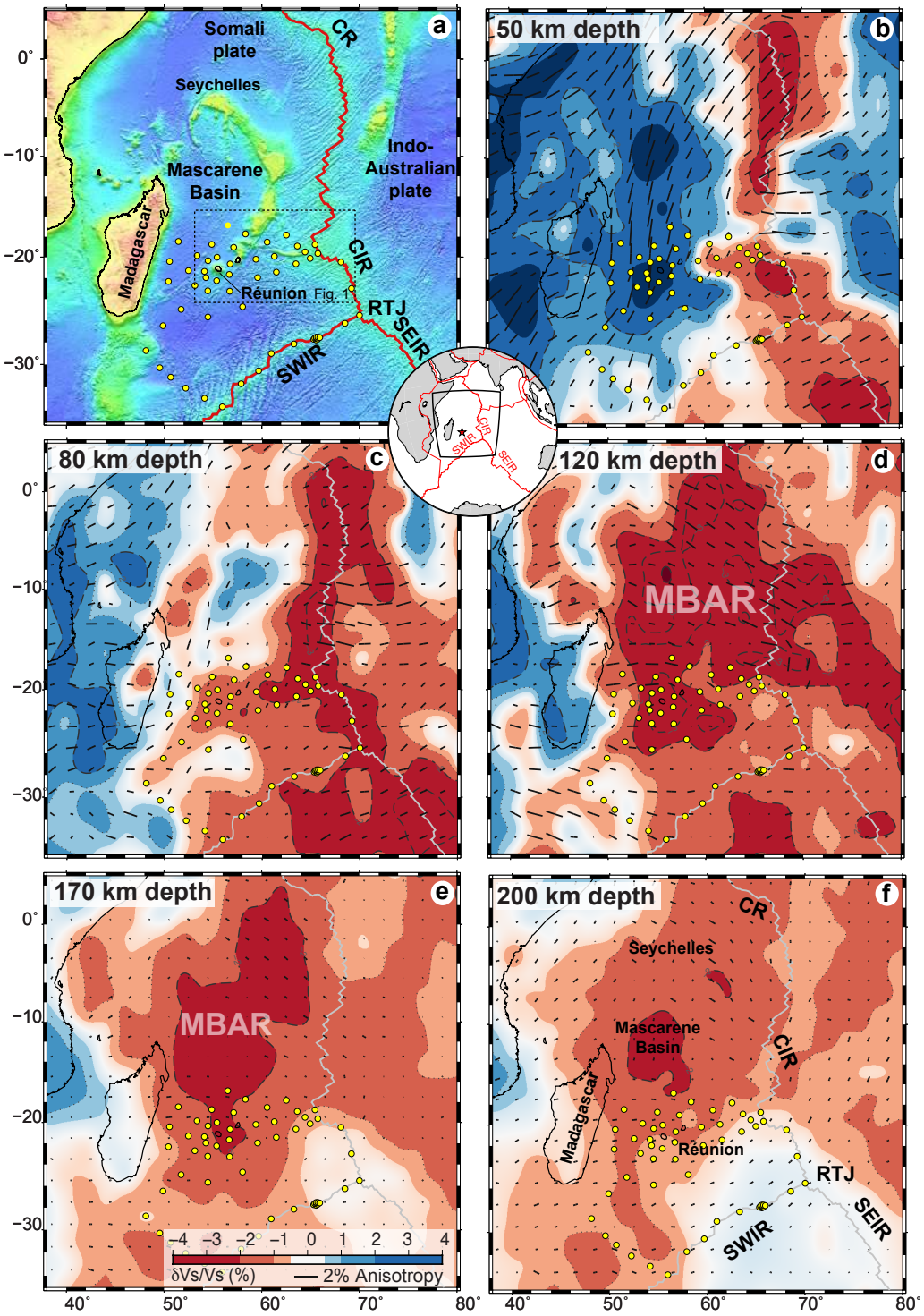

a
Somali plate
Seychelles
Mascarene Basin
Indo-Australian plate
Madagascar
Réunion
Fig. 1
CR
CIR
RTJ
SEIR
SWIR
b
50 km depth
c
80 km depth
d
120 km depth
MBAR
e
170 km depth
MBAR
f
200 km depth
Seychelles
Mascarene Basin
Madagascar
Réunion
CR
CIR
RTJ
SEIR
SWIR
−4 −3 −2 −1 0 1 2 3 4
δVs/Vs (%)
2% Anisotropy
0°
−10°
−20°
−30°
40°
50°
60°
70°
80°

Figure 2

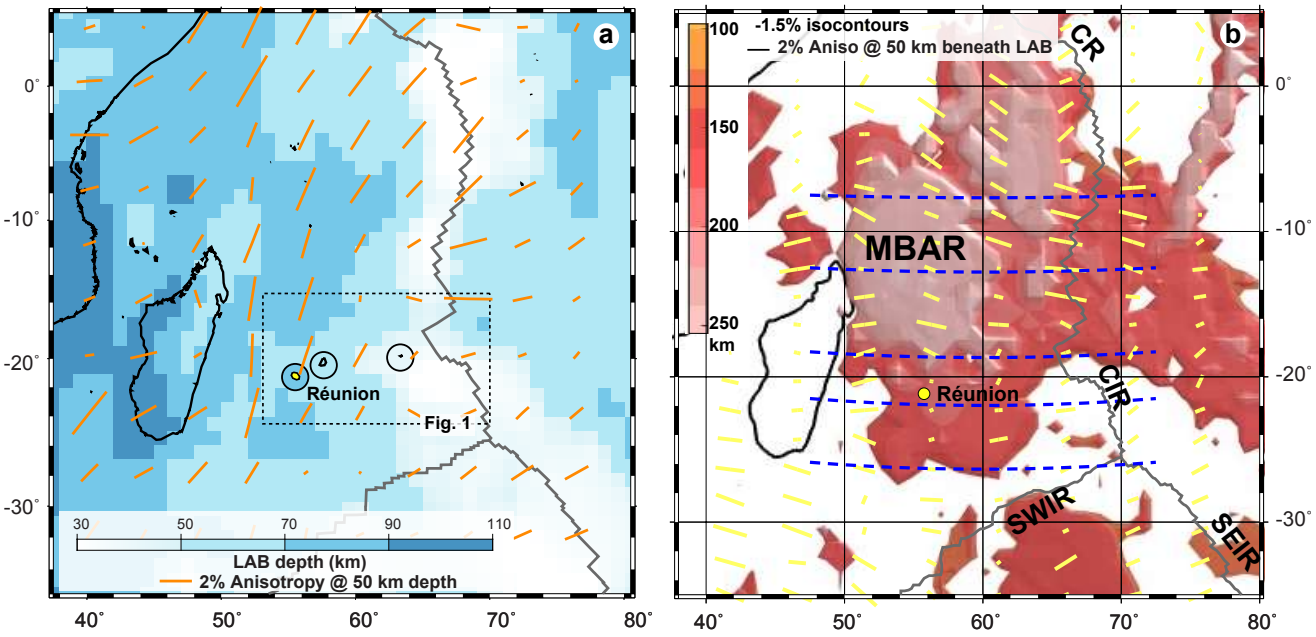

a
b
Réunion
Fig. 1
LAB depth (km)
2% Anisotropy @ 50 km depth
-1.5% isocontours
2% Aniso @ 50 km beneath LAB
MBAR
CR
CIR
SWIR
SEIR
km
0˚
-10˚
-20˚
-30˚
40˚
50˚
60˚
70˚
80˚

Figure 3

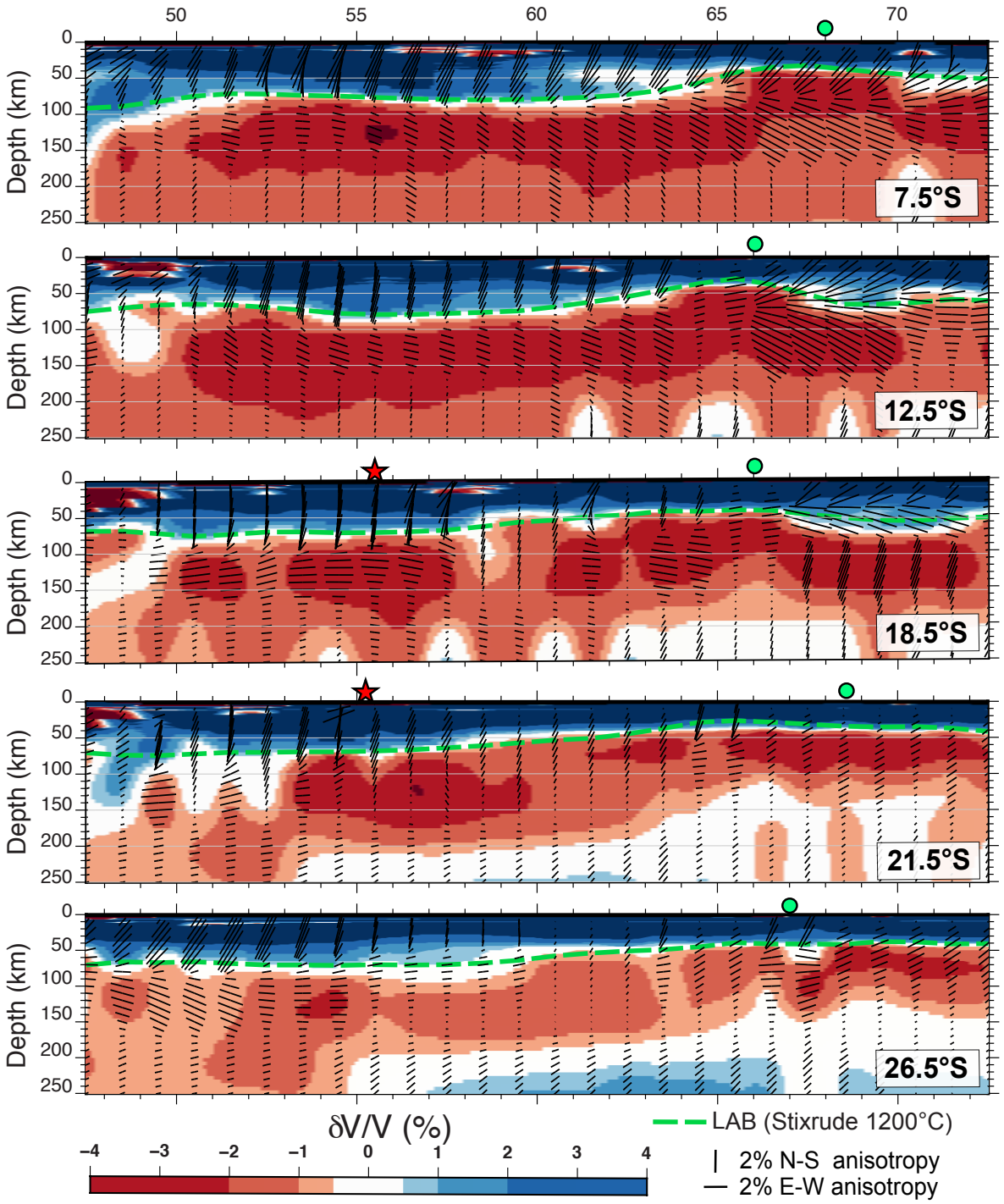

50
55
60
65
70
Depth (km)
0
50
100
150
200
250
7.5°S
12.5°S
18.5°S
21.5°S
26.5°S
δV/V (%)
−4
−3
−2
−1
0
1
2
3
4
LAB (Stixrude 1200°C)
2% N-S anisotropy
2% E-W anisotropy

Figure 4

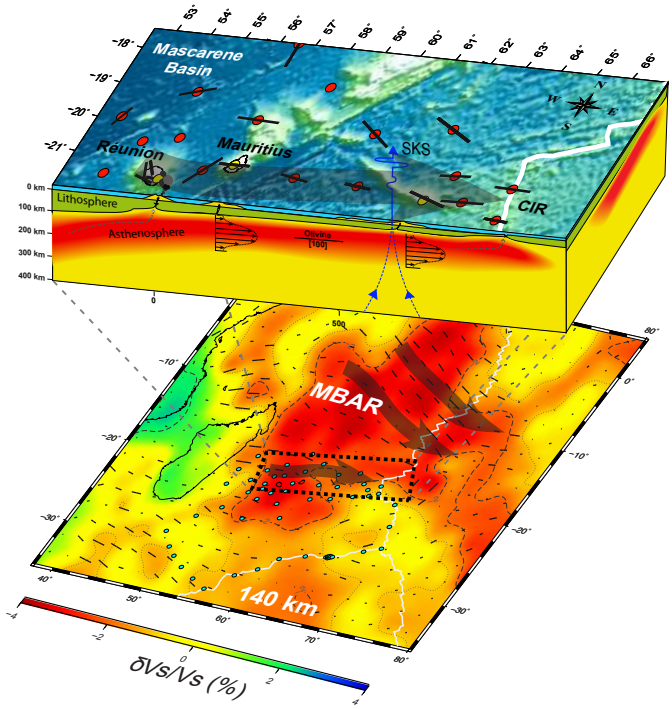

Mascarene Basin
Réunion
Mauritius
SKS
CIR
Lithosphere
Asthenosphere
Olivine [100]
MBAR
140 km
δVs/Vs (%)

Figure 5

Large-scale flow of Indian Ocean asthenosphere driven by Réunion plume

G. Barruol*[1,2], K. Sigloch[3], J.-R. Scholz[1,2], A. Mazzullo[1], E. Stutzmann[1], J.-P. Montagner[1], S. Kiselev[4], F. R. Fontaine[1,2], L. Michon[1,2], C. Deplus[1], J. Dyment[1]

1. Université de Paris, Institut de physique du globe de Paris, CNRS, UMR 7154, F-75005 Paris, France

2. Université de La Réunion, Laboratoire GéoSciences Réunion, F-97744 Saint Denis, France

3. University of Oxford, Earth Sciences Department, South Parks Road, Oxford OX1 3AN, UK.

4. Institute of Physics of the Earth, Moscow, Russia

SUPPLEMENTARY INFORMATION (SI)

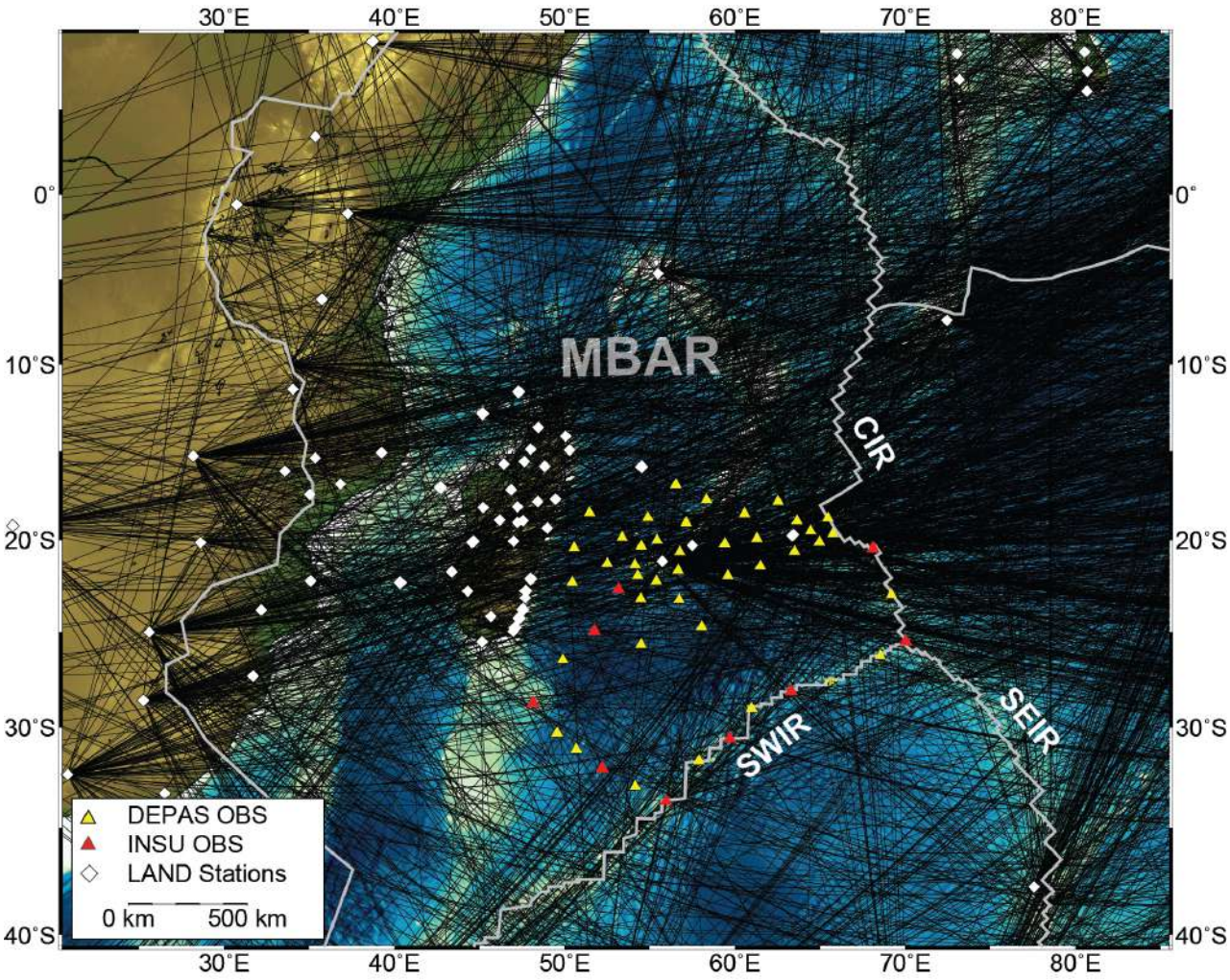


Figure S1

Figure S1: Map of the South-West Indian Ocean showing the RHUM-RUM network, including the German DEPAS OBS (yellow triangles) and the French INSU OBS (red triangles) stations deployed around Réunion, along the Central Indian Ridge (CIR) and the South-West Indian Ridge (SWIR). Also shown are the terrestrial seismic stations used (white diamonds), and the corresponding ray coverage used in the RHUM-RUM surface wave tomography[1]. "MBAR" indicates the centre of the Mascarene Basin Asthenosphere Reservoir discussed in the paper.

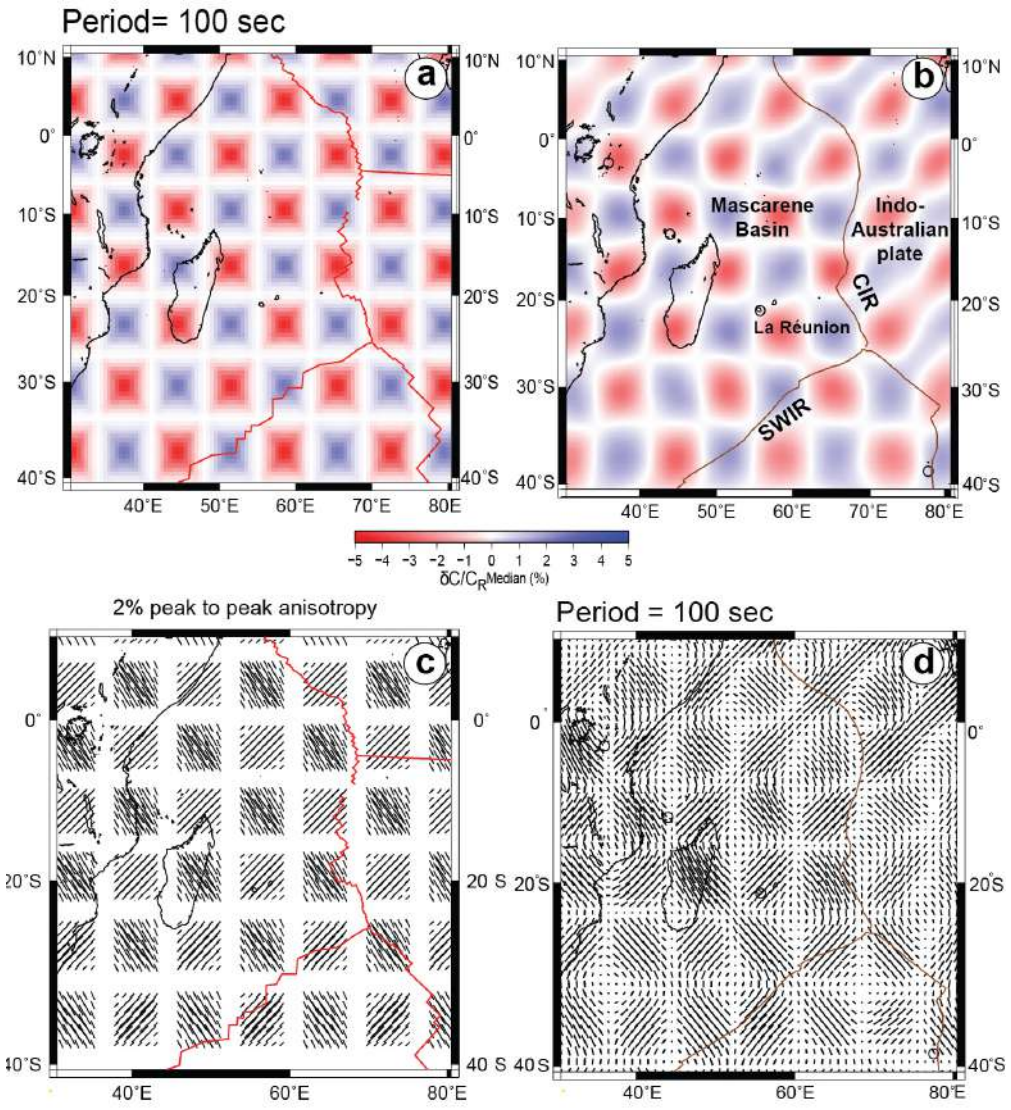


Figure S2

Figure S2: Synthetic tomography resolution test performed at 100s period. Left panels, we show the input velocity (a) and anisotropy structures (c). On the right panels, we show their respective recovery (b and d) from our actual ray coverage (Fig. S1). The slow and fast velocity structure, together with the azimuthal anisotropy pattern, are well recovered, particularly around Réunion, the Central Indian Ridge, and over the whole Mascarene Basin Asthenospheric Reservoir area (Fig. S1).

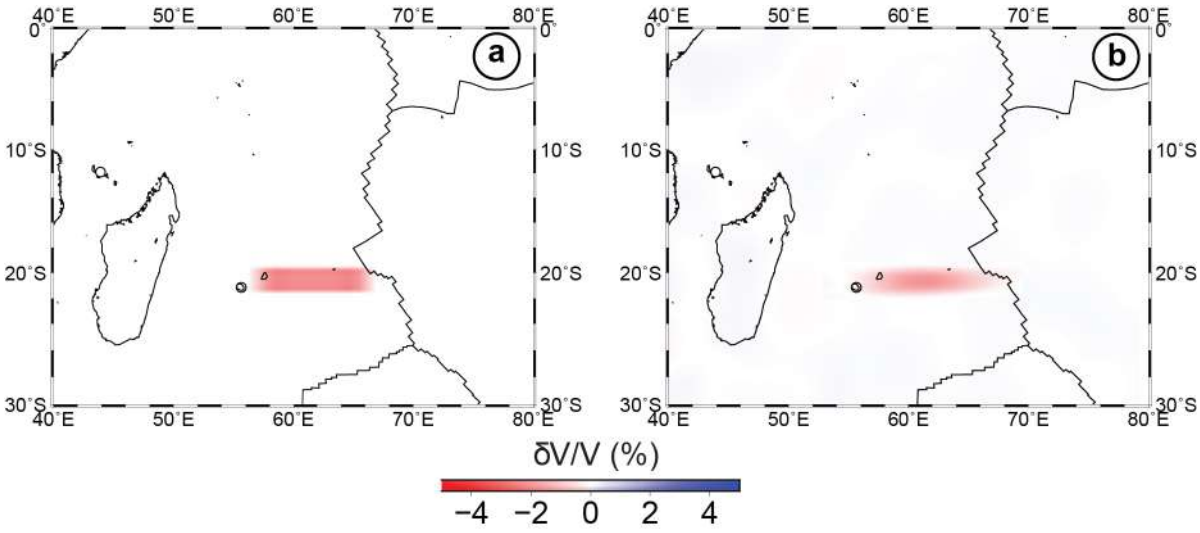


Figure S3

Figure S3: Synthetic tomography resolution test below the Rodrigues corridor. (a) Input is a slow velocity structure (*dVs/Vs* = -3%), sized 200km x 1000km, resembling the channel of slow asthenosphere present in the actual tomography model. (b) Resolution test output recovers the input well, with some smearing in east-west direction.

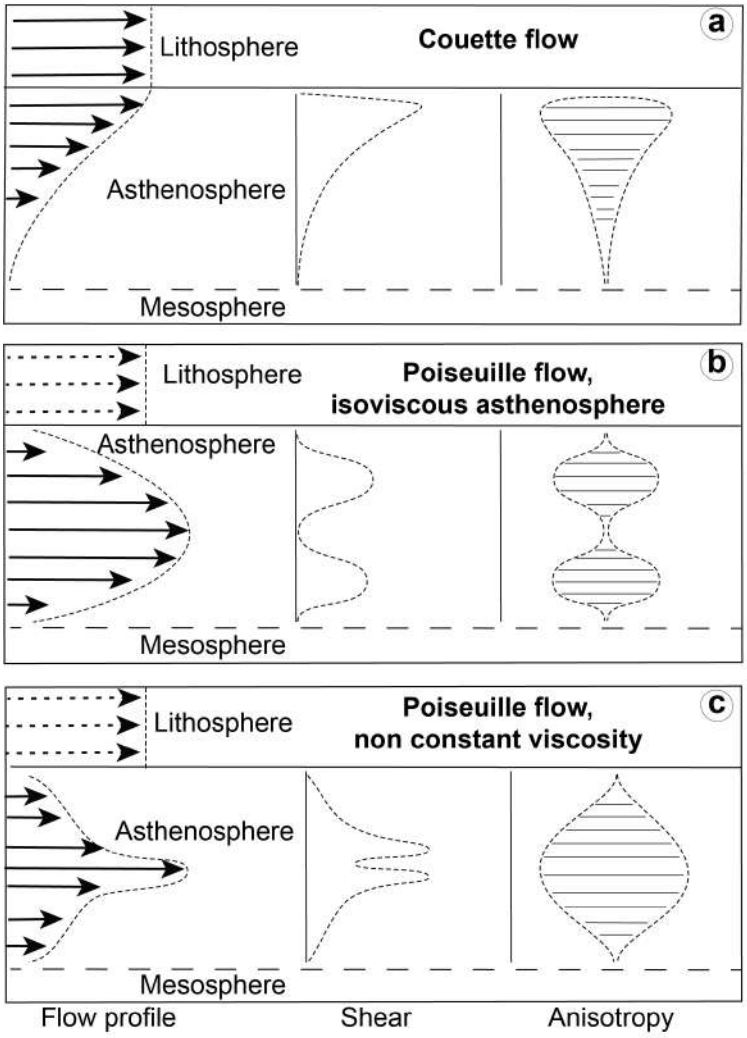


Figure S4

Figure S4: Development of anisotropy in the asthenosphere as a consequence of planar horizontal flow. In all panels, depth is plotted on the y-axis, showing a lithospheric layer above an asthenospheric layer ending at the asthenosphere-mesosphere boundary. Left panels: arrows show horizontal flow velocities as a function of depth. Middle panels: magnitude of shear strain as a function of depth. Right panels: magnitude of azimuthal anisotropy as a function of depth. The seismically fast direction is horizontal, the seismically slow direction is into and out of the figure plane.

(a) Couette flow: asthenosphere is passively dragged by the overlying lithosphere, which moves from left to right. Resulting strain and anisotropy are proportional to the vertical derivative of flow velocity, and peak just below the LAB. (b) Planar Poiseuille flow in an iso-viscous asthenosphere: a horizontal pressure gradient (from left to right) actively drives

horizontal flow in the asthenosphere. Lithosphere and asthenosphere are decoupled, i.e., lithospheric motion exerts no influence on flow in the asthenosphere. The asthenosphere is also decoupled from the underlying mesosphere. Strain and anisotropy have two well-separated lobes. (c) Poiseuille-like flow in a non-linear, mantle-like rheology: like case b), except that viscosity decreases towards the middle of the asthenosphere. This concentrates not only flow in the middle of the layer, but also its derivative, and therefore strain and anisotropy.

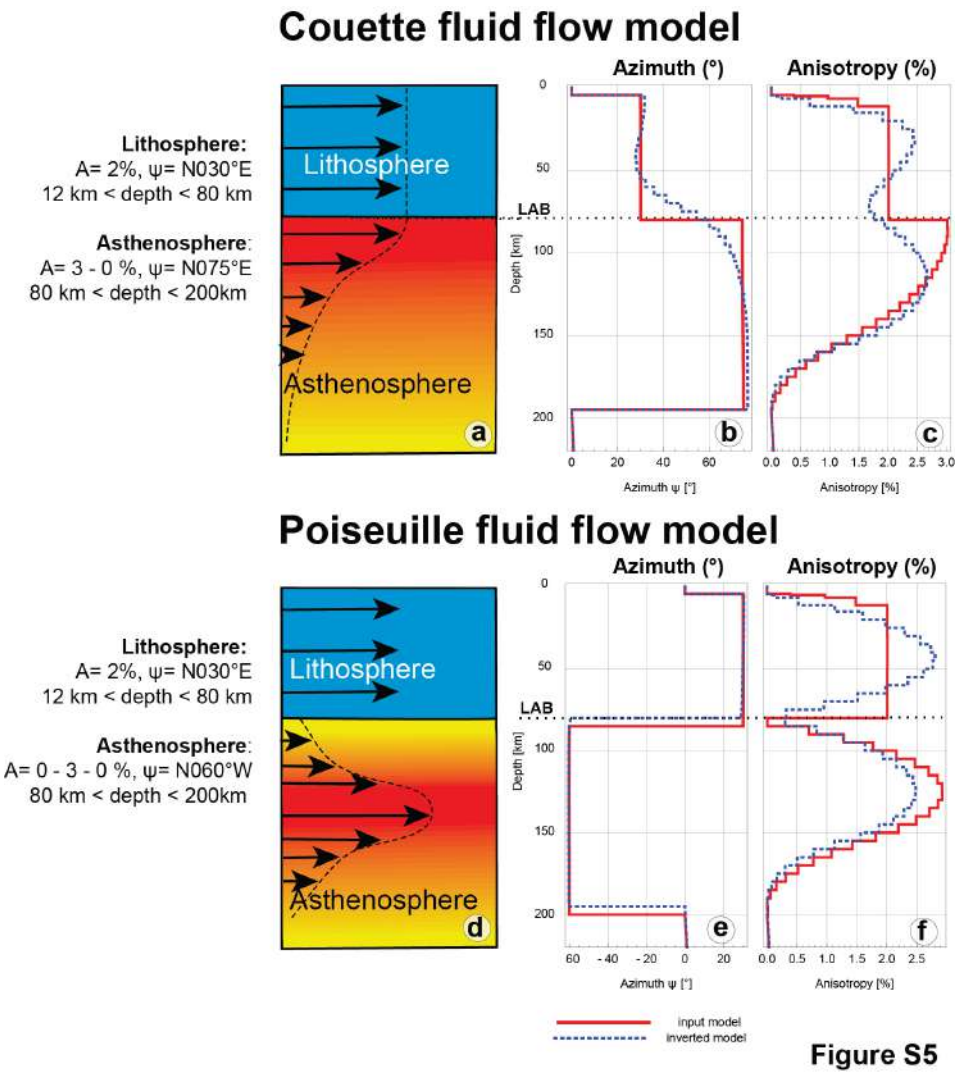


Figure S5: Tomographic resolution tests for the vertical distribution of anisotropy for the scenarios of planar Couette flow (top), and of planar Poiseuille flow in an asthenosphere that is weakest in the middle of the layer (bottom). The structure of fluid flow in each case is illustrated by panels (a) and (d). Lithosphere is shown in blue; in the asthenosphere, red regions support the highest shear and yellow regions are shearing less. Panels (b) and (e) show the seismically fast direction of azimuthal anisotropy as a function of depth: test inputs in red, recovered results in blue. Panels (c) and (f) show the magnitude of azimuthal anisotropy as a function of depth: inputs in red, recovered results in blue.

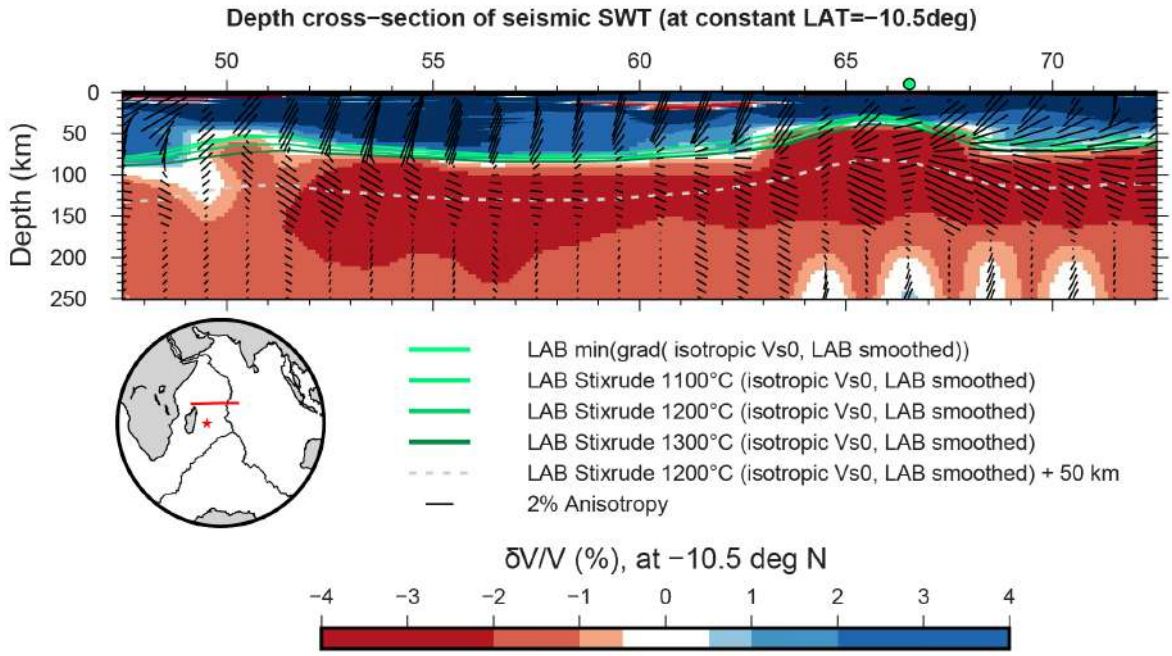


Figure S6

Figure S6: Estimating LAB depth. East-west cross section at 10.5°S through the Rayleigh wave tomography model of Mazzullo et al. (2017)[1], plotting styles as in main Fig. 4. Four lines in different shades of green represent different estimates of the lithosphere-asthenosphere boundary. Lightest green line traces the location of the steepest vertical gradient in isotropic *dVs/Vs* (Method 1). Three other green lines are LAB depths based on estimating the locations of the 1100°C, 1200°C and 1300°C isotherms[2] (Method 2). White dashed line runs 50 km below the estimated 1200°C isotherm[2], a rough estimate for the middle of the asthenospheric layer, which is used to plot azimuthal anisotropy on Fig. 3b.

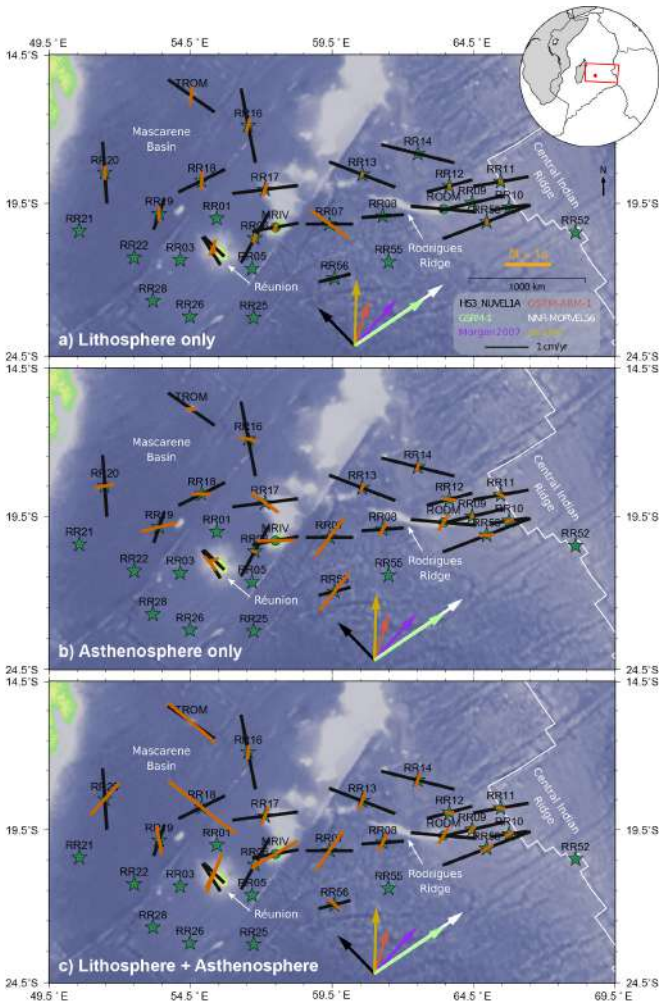


Figure S7

Figure S7: Observed versus tomography-predicted SKS splitting. Black bars are station-averages of measured SKS splitting parameters[3] in the area around the Réunion hotspot (red dot on inset map), Rodrigues corridor and Central Indian Ridge; orange bars are SKS splitting parameters forward-predicted through our Rayleigh-wave tomography model. SKS predictions were calculated for (a) only the lithosphere (25 km depth to LAB); (b) only the asthenosphere (LAB to 300 km depth); and (c) for the whole lithosphere + asthenosphere system (25 to 300 km depth). Coloured arrows indicate African (Somali) plate motion according to models HS3_NUVEL1A[4], GSRM-1[5], Morgan2007[6], GSRM-ARM-1[7], NNR-MORVEL56[8], and SA-APM[9]. First-order features are a general under-prediction of delay time magnitudes; good overall agreement between observed and predicted fast directions in the asthenosphere; and for the Rodrigues corridor, much larger delay times predicted for the asthenosphere than for the lithosphere, supporting the interpretation of anisotropy reflecting flow beneath the corridor.

References

1. Mazzullo A.*, et al.* Anisotropic Tomography around La Réunion Island from Rayleigh Waves. *J. Geophys. Res.*, **122**, 1-17 (2017).
2. Stixrude L. & Lithgow-Bertelloni C. Mineralogy and elasticity of the oceanic upper mantle: Origin of the low-velocity zone. *J. Geophys. Res.*, **110**, B03204 (2005).
3. Scholz J.-R.*, et al.* SKS splitting in the Western Indian Ocean from land and seafloor seismometers: Plume, Plate and Ridge signatures. *Earth Planet. Sci. Lett.*, **498**, 169-184 (2018).
4. Gripp A.E. & Gordon R.B. Young tracks of hotspots and current plate velocities. *Geophys. J. Int.*, **150**, 321-361 (2002).
5. Kreemer C., Holt W.E. & Haines A.J. An integrated global model of present-day plate motions and plate boundary deformation. *Geophys. J. Int.*, **154**, 8-34 (2003).
6. Morgan W.J. & Morgan J.P. Plate velocities in the hotspot reference frame. In: Foulger GR, Jurdy DM (eds). *Plates, plumes, and planetary processes*, vol. 430. Geological Society of America Special Paper, pp 65-78 (2007).
7. Kreemer C. Absolute plate motions constrained by shear wave splitting orientations with implications for hot spot motions and mantle flow. *J. Geophys. Res.*, **114**, B10405 (2009).
8. Argus D.F., Gordon R.G. & DeMets C. Geologically current motion of 56 plates relative to the no-net-rotation reference frame. *Geochem. Geophys. Geosyst*, **12**, Q11001 (2011).
9. Becker T.W., Schaeffer A.J., Lebedev S. & Conrad C.P. Toward a Generalized Plate Motion Reference Frame. *Geophys. Res. Lett.*, **42**, 3188-3196 (2015).
10. Seton M.*, et al.* Global continental and ocean basin reconstructions since 200Ma. *Earth-Science Reviews*, **113**, 212-270 (2012).
11. Wolfe C.J. & Solomon S.C. Shear wave splitting and implication for mantle flow beneath the MELT region of the East Pacific Rise. *Science*, **280**, 1230-1232 (1998).
12. Stotz I.L., Iaffaldano G. & Davies D.R. Pressure-Driven Poiseuille Flow: A Major Component of the Torque-Balance Governing Pacific Plate Motion. *Geophys. Res. Lett.*, **45**, 117-125 (2018).
13. Debayle E. & Ricard Y. Seismic observations of large-scale deformation at the bottom of fast-moving plates. *Earth Planet. Sci. Lett.*, **376**, 165-177 (2013).
14. Takeo A.*, et al.* Seismic azimuthal anisotropy in the oceanic lithosphere and asthenosphere from broadband surface wave analysis of OBS array records at 60 Ma seafloor. *J. Geophys. Res.*, **121**, 1927–1947 (2016).
15. Natarov S.I. & Conrad C.P. The role of Poiseuille flow in creating depth-variation of asthenospheric shear. *Geophys. J. Int.*, **190**, 1297-1310 (2012).